Optimal Lateral Guidance for Automatic Landing of a Lightweight High Altitude Long Endurance Unmanned Aerial System with Crosswind Rejection

By

Nathanial Allen Smith

Submitted to the graduate degree program in Aerospace Engineering and the Graduate Faculty of the University of Kansas in partial fulfillment of the requirements for the degree of Master of Science.

Date Defended: 08/29/2016

The Thesis Committee for Nathanial Allen Smith

certifies that this is the approved version of the following thesis:

Optimal Lateral Guidance for Automatic Landing of a Lightweight High Altitude Long Endurance Unmanned Aerial System with Crosswind Rejection

_____

Chairperson Dr. Shawn Keshmiri

Date approved:

Abstract

Unmanned aerial systems will be the dominant force in the aviation industry. Among these aircraft the use of high altitude long endurance unmanned aerial systems has increased dramatically. Based on the geometry of these types of aircraft the possible changing weather conditions during long flights poses many problems. These difficulties are compounded by the push towards fully autonomous systems. Large wingspan and, typically, small in-line landing gear make a landing in crosswind exceedingly difficult. This study uses a modified gain scheduling technique for optimizing the landing attitude for a generic vehicle based on geometry and crosswind speed. This is performed by directly utilizing the crosswind estimation to calculate a desired crab and roll angle that gives the lowest risk attitude for landing. An extended Kalman filter is developed that estimates the aircraft states as well as the 3D wind component acting on the aircraft. The aircraft used in this analysis is the DG808S, a large wingspan lightweight electric glider. The aircraft is modelled using Advanced Aircraft Analysis software and a six degree of freedom nonlinear simulation is implemented for testing. The controller used is a nonlinear model predictive controller. The simulations show that the extended Kalman filter is capable of estimating the crosswind and can therefore be used in the full aircraft simulation. Different crosswind settings are used which include both constant crosswind and gust conditions. Crosswind landing capabilities are increased by 35%. Deviation from the desired path in the cruise phase is reduced by up to 68% and time to path convergence is reduced by up to 53%.

Acknowledgements

I would like to thank Dr. Shawn Keshmiri for his support and help through this process, especially when things got tough and I was foolish enough to think I could handle raising a new born along with school, CReSIS, flight testing and research. He stood by me and understood when I was in over my head. I would like to thank Bella Kim for being a great coworker and researcher. She would help me succeed and find any answers I was searching for, as well as being an ear for me to vent to in troubling times. I would like to thank Dr. Gonzalo Garcia for being a great teacher and researcher and helping me navigate the NMPC and Simulink. His development of the NMPC and autopilot used in this research was invaluable. I would like to thank Dr. Mark Ewing for guiding me through undergraduate school and CReSIS. I would like to thank Wes Ellison for giving me a chance and allowing me to gain great experience as an undergrad. Lastly I would like to thank my wife, Megan, for working so hard to support me and our family while on this journey.

Table of Contents

List of Figures

Page #

List of Tables

Page #

Chapter 1

Introduction

As aerospace systems move closer to fully autonomous, the need for accurate automatic landing increases. One third of aircraft accidents at landing are directly due to adverse wind conditions [1]. This number occurs when piloted aircraft are using the standard landing techniques. Many UAS autopilots do not directly command lateral attitude using crosswind conditions [2, 3]. An attitude is determined based on the error from the current state and trajectory to the desired state and trajectory. The aircraft studied here are high endurance and are typically out of range of a ground pilot. Any adversity must be handled autonomously. A guidance technique to handle changing weather conditions and an accurate landing approach would be beneficial in an emergency as well as during typical flight operations.

High altitude long endurance (HALE) aircraft have been studied for many years and are now entering service as unmanned aerial systems (UAS) [4]. These aircraft utilize a lightweight high aspect ratio design that is highly susceptible to adverse wind conditions. They can stay in the air for several days studying hurricanes or surveying boarders for a few examples. The wide use today and expected use in the future calls for autonomous landing. This provides safety in the event of an emergency landing in the field or if an unsupervised landing is required.

To understand how an aircraft is impacted by wind, the wind itself must be understood. Due to wind being both special and temporal, this is not an easy task, however, recently there have been many advancements in this area. Many studies have been completed to derive methods of predicting wind behavior. NASA has a complex model for wind that was derived from

many years of observation from the United States Department of Defense and many academic institutions spanning the 1970's and 1980's [5, 6]. More recently spatio-temporal correlation methods have been developed based on the large amounts of data using Bayesian dynamic modeling [7, 8, 9]. These models predict the wind based on the three dimensional correlated components and are becoming increasingly accurate. In an effort to better understand the wind conditions as a function of altitude, more recent studies have shown that a positive gradient relative to height exists [10]. This is important for energy savings in flight, especially powerless flight, and in the wind energy generation field.

This autonomy is not only useful in near ground operations. New, more advanced, sensors and controllers are being used that allow aircraft to operate in close proximity while remaining autonomous in cruise flight. The proximity is, however, limited by the response of the aircraft to wind conditions. A cruise guidance that directly responds to crosswind effects by inducing a coordinated turn into the wind will reduce the time to recover from un-commanded disturbances.

Many automatic landing guidance systems do not use crosswind to directly determine the aircraft lateral or directional attitude [2, 3]. The lateral and directional control of the autopilot is left to handle the effects without direct attitude command relative to the crosswind component. This limits the flight envelope for the landing sequence of an aircraft when only the error in the trajectory is used. This leads to either the directional orientation of the aircraft being misaligned with the runway or the aircraft not being leveled upon landing. In low wind conditions this is allowable and, depending on the geometric limits of the aircraft, may be allowable for higher wind. However, this is not ideal for lightweight aircraft with large wingspan or low wing aircraft

with little dihedral. For these aircraft limiting factors, such as, roll and crab angle must be taken into account. An aircraft with high wingspan is susceptible to wingtip strike upon landing in gusty conditions. An aircraft with in-line landing gear cannot land with a crab angle without rolling upon touchdown, possibly damaging the aircraft. Drift must be considered when de-crabbing the aircraft directly prior to touchdown. A high aspect ratio aircraft is susceptible to ground effects and floating may occur, causing the aircraft to remain in the air longer than desired [10, 11]. This would allow the aircraft to drift off course and could result in a dangerous landing for both the aircraft and any ground crew or other vehicles.

Small changes in the wind field surrounding these aircraft can cause dramatic changes in the aircraft orientation and position [12]. It is important that the aircraft maintain course and landing capabilities in these conditions. Many times, research must be halted on days when the wind is only at moderate levels. For the HALE aircraft, adverse weather conditions could arise during long flight times. Combining wind estimation with robust control, and a guidance system utilizing the wind, can increase the flight envelope while decreasing the time for trajectory convergence and allow for accurate and safe landings.

Many automatic landing algorithms have been completed and successfully tested. Though wind estimation is used and included in the dynamic equations, these flight controllers do not typically control any lateral or directional dynamics based specifically on crosswind for landing. Most use an extended Kalman filter wind estimator to more accurately model the un-commanded disturbances and rely solely on the controller to correct any disturbances [13, 14].

Many high level controllers are used successfully for automatic landing. Quantitative feedback, time delay, fuzzy logic, along with standard successive loop closure, L_1adaptive

control, proportional feedback, linear parameter varying and neurocontrollers are used [15, 16, 17, 18, 19, 20, 21]. In each of these cases the controller is manipulating the attitude for best trajectory tracking while a longitudinal guidance is landing the aircraft. No lateral directional attitude is commanded based solely on the crosswind estimation.

For more accuracy on landing some controllers compensate for ground effects [22]. Approach time and landing distance are optimized to meet short landing requirements as well as landing on mobile platforms [23, 24]. Varying glideslopes are used with neurocontrollers for autolanding [21].

Slowing the aircraft and landing in a net has also been successfully accomplished [25]. These require either low wind conditions or a controller that accurately compensates for crosswind. Most of these methods use error feedback alone to model the un-commanded disturbances. These controllers are robust and allow for error within the system. The robustness of the controller used in this study also helps with the wind gusts [26]. The two together allow the aircraft to land in high crosswind and gust conditions. Robust controllers are able to overcome variations from expectations but also allow for larger margins of error. Wind is one of these variations. Linear controllers can overcome small variations but nonlinear robust control can overcome much greater variations. This helps small UAS's landing during wind shear, however there is a limit to the orientation that an aircraft can have upon landing. Employing a guidance that accounts for this change as well as using a nonlinear robust controller will increase the landing ability in crosswind conditions.

To increase robustness during the landing and takeoff phases different techniques have been utilized including minimizing the error from the flight path using perpendicular distance and

velocity rather than relying on waypoints. This gives a more accurate flight path for some small UAVs [26]. The use of waypoints with closed loop image processing from a gimballed camera is also used to increase robustness [27, 28, 29].

HALE aircraft are typically in the air for long periods. They also may travel long distances out of sight or far from a safe landing zone. For these reasons a safe and reliable landing guidance is needed. Landing guidance for impaired aircraft has been formulated as well as emergency procedures [30, 31]. These procedures coupled with laterally controlled aircraft attitude would help ensure safer landings and recovery of the aircraft.

There are a few autopilots that adjust the attitude based on crosswind. One way to increase the accuracy for lateral directional path following in crosswind is a sliding mode approach. This approach using crosswind is incorporated into the formulation along with gains and a feedforward component related to the rate of change of the desired path [32]. Crosswind estimation is used in a crab/de-crab approach along with active disturbance rejection control to simulate the safe landing of a large wingspan aircraft [33]. Similarly this research uses gains to make small corrections to the aircraft attitude to help in rejecting wind disturbances. A sideslip angle is calculated based on an optimally chosen gain for the expected crosswinds in both cruise and landing phases of flight. This gain forces the aircraft into a roll maneuver effectively create a coordinated turn to compensate for the crosswind. The crosswind is estimated using an extended Kalman filter. The EKF estimates all states for increased accuracy if need. It also estimates the three dimensional wind components.

For aircraft with two wheels, in-line, which is the case for many high endurance gliding aircraft, a de-crab maneuver cannot be performed after touchdown. For the DG808S the wheels

are in line and this would cause the aircraft to roll upon landing possibly damaging the aircraft. A sideslip landing approach is more suited for this aircraft since it is not able to touchdown at an angle. However, this raises difficulties as well. The DG808S, which is similar to these aircraft, has a four meter wingspan and the wings are only eight inches off the ground. A roll angle is required to compensate for the crosswind, so there is a maximum roll angle that may be achieved without damaging the aircraft. The best result would be a combination that would allow the aircraft to land while reducing the yaw angle by maintaining a roll angle that is below a defined threshold. This attitude should be controlled in a manner that allows the controller full authority and does not diminish performance.

Chapter 2

Kinematics, Dynamics and DG808S Geometry and Modeling

The NMPC is a model-based controller. An accurate dynamic model must be created for this controller to work properly. The dynamic model is the on board mathematical description of the aircraft. It accepts the measurements and generates the outputs to command the control surfaces that guide the aircraft to the desired path or location. An inaccurate dynamic model will cause the control surfaces to guide the aircraft incorrectly, in the best case resulting in oscillations and in the worst case complete failure. The model for the DG808S is created using Advanced Aircraft Analysis software (AAA). The flight dynamics and modeling theory is provided in sections 2.1 through 2.3. The aircraft geometry and flight characteristics are given in section 2.4.

2.1 Coordinate systems

Four coordinate systems are used for autonomous UAS flight. The inertial coordinate system is earth based with axis North, East and down. The body coordinate system is positioned at the aircraft center of mass with the x axis positive out the nose, the y axis positive out the right wing and the z axis positive down. The stability coordinate system is positioned at the aircraft center of mass with the positive x axis pointed into the oncoming longitudinal angle for wind and the y axis at a right angle to the right and the z axis at a right angle to x and y, down. This coordinate system is used only when sideslip is assumed zero. The wind coordinate system is the stability system when sideslip is taken into account, therefore producing longitudinal and lateral directional forces. A non-inertial wind frame may also be considered a dynamic frame and this is called the air-mass-relative frame. The coordinate systems are represented in figure 1.

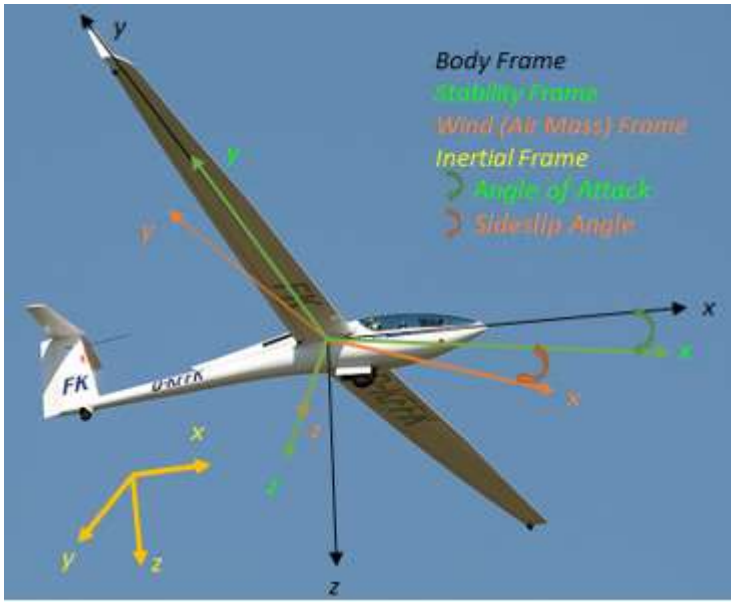

Figure 1: Coordinate Reference Frames [34].

These four coordinate systems are in Euclidean space and can be represented in each of the other systems using the following coordinate transformations:

$$R_b^I = \begin{bmatrix} cos\theta cos\psi & sin\phi sin\theta cos\psi - cos\phi sin\psi & cos\phi sin\theta cos\psi + sin\phi sin\psi \\ cos\theta sin\psi & sin\phi sin\theta sin\psi + cos\phi cos\psi & cos\phi sin\theta sin\psi - sin\phi cos\psi \\ -sin\theta & sin\phi cos\theta & cos\phi cos\theta \end{bmatrix} \quad [2.1]$$

$$R_w^b = \begin{bmatrix} cos\beta cos\alpha & -sin\beta cos\alpha & -sin\alpha \\ sin\beta & cos\beta & 0 \\ cos\beta sin\alpha & -sin\beta sin\alpha & cos\alpha \end{bmatrix} \quad [2.2]$$

These transformation matrices are orthogonal and may be inverted by using the transpose.

$$R_b^I = R_I^{b^T}, R_w^b = R_b^{w^T} \quad [2.3]$$

The calculations for the aerodynamic forces and moments are simplified when calculating them directly in the air-mass-relative frame [35]. The air relative velocity vector of the aircraft is:

$$V_A = V_I - w = \begin{bmatrix} v_1 \\ v_2 \\ v_3 \end{bmatrix} - \begin{bmatrix} w_1 \\ w_2 \\ w_3 \end{bmatrix} \quad [2.4]$$

Using the body frame with the wind direction chosen as to increase in the case of headwind the aircraft velocity in the body frame is represented by:

$$[V_A]_b = \begin{bmatrix} u_A \\ v_A \\ w_A \end{bmatrix} = R_I^b V_A = V_b - R_I^b w \quad [2.5]$$

$$V_A = \sqrt{u_A^2 + v_A^2 + w_A^2} \quad [2.6]$$

$$\alpha_A = \tan^{-1} \frac{w_A}{u_A} \quad [2.7]$$

$$\beta_A = \sin \frac{v_A}{\sqrt{u_A^2 + v_A^2 + w_A^2}} \quad [2.8]$$

These definitions of V, α and β are used to calculate the aerodynamic forces and moments presented in section 2.2 [35].

The NMPC commands pitch angle based on the trim values given from the dynamic model. Sideslip is commanded to zero allowing the yaw angle to be set by heading in the commanded direction and minimizing drag from outside disturbances. The alternate form will provide a function for commanding sideslip to create a situation where the disturbances must be rejected using other control surfaces. In this case aileron will be used to counter crosswind in coordination with rudder. The sideslip command is the opposite estimation with a proportional gain given in equation 2.9.

$$\beta = -K_\beta \sin \frac{v_A}{\sqrt{u_A^2 + v_A^2 + w_A^2}} \quad [2.9]$$

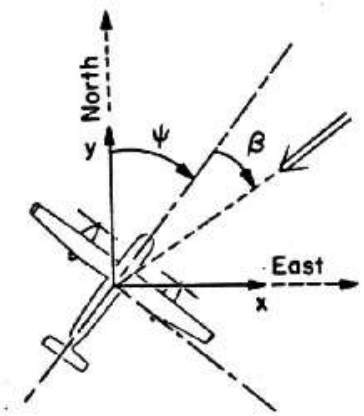

Figure 2: Sideslip of Aircraft in Crosswind (36)

From figure 2 it can be seen that if sideslip is commanded then the angle between the heading and aircraft x_b will decrease. In the case of landing this will decrease the crab angle. A roll angle will be introduced to compensate for the crosswind. This formulation is the driving force behind this research and will be discussed in detail in chapter 6.

2.2 Aerodynamic Forces and Moments

As discussed in the previous section the aerodynamic forces and moments act in the air-mass-relative reference frame. The propulsive force acts in the body frame and the gravitational force acts in the inertial frame. The total forces acting on the aircraft are represented by the sum of the gravitational, aerodynamic and propulsive forces.

$$f = f_g + f_a + f_p \quad [2.10]$$

The total moments acting on the aircraft are represented by the sum of the aerodynamic and propulsive forces.

$$m = m_a + m_p \quad [2.11]$$

The gravitational force is represented in equation 2.12 in the inertial system and transferred to the body frame in equation 2.13.

$$f_g^I = \begin{bmatrix} 0 \\ 0 \\ mg \end{bmatrix} \quad [2.12]$$

$$f_g^b = R_I^b f_g^I = \begin{bmatrix} -mgsin\theta \\ mgcos\theta sin\phi \\ mgcos\theta cos\phi \end{bmatrix} \quad [2.13]$$

The forces and moments are separated into two groups, the longitudinal and the lateral directional aerodynamics. The forces of lift, drag, and the pitching moment are longitudinal and are represented by the following equations:

$$f_{lift} = \frac{1}{2}\rho V_a^2 S C_L(\alpha, q, \delta_e) = \bar{q}S\left[C_{L_0} + C_{L_\alpha}\alpha + \frac{C_{L_q}c}{2V_a}q + C_{L_{\delta_e}}\delta_e\right] \quad [2.14]$$

$$f_{drag} = \frac{1}{2}\rho V_a^2 S C_D(\alpha, q, \delta_e) = \bar{q}S\left[C_{D_0} + C_{D_\alpha}\alpha + \frac{C_{D_q}c}{2V_a}q + C_{D_{\delta_e}}\delta_e\right] \quad [2.15]$$

$$m = \frac{1}{2}\rho V_a^2 S C_m(\alpha, q, \delta_e) = \bar{q}Sc\left[C_{m_0} + C_{m_\alpha}\alpha + \frac{C_{m_q}c}{2V_a}q + C_{m_{\delta_e}}\delta_e\right] \quad [2.16]$$

The side force, rolling and yawing moments are lateral directional and are represented by the following equations:

$$f_y = \frac{1}{2}\rho V_a^2 S C_Y(\beta, p, r, \delta_a, \delta_r) = \bar{q}S\left[C_{Y_0} + C_{Y_\beta}\beta + \frac{C_{Y_p}b}{2V_a}p + \frac{C_{n_r}b}{2V_a}r + C_{Y_{\delta_a}}\delta_a + C_{Y_{\delta_r}}\delta_r\right] \quad [2.17]$$

$$l = \frac{1}{2}\rho V_a^2 S C_l(\beta, p, r, \delta_a, \delta_r) = \bar{q}S\left[C_{l_0} + C_{l_\beta}\beta + \frac{C_{l_p}b}{2V_a}p + \frac{C_{n_r}b}{2V_a}r + C_{l_{\delta_a}}\delta_{a+}C_{l_{\delta_r}}\delta_r\right] \quad [2.18]$$

$$n = \frac{1}{2}\rho V_a^2 S C_n(\beta, p, r, \delta_a, \delta_r) = \bar{q}Sc\left[C_{n_0} + C_{n_\beta}\beta + \frac{C_{n_p}b}{2V_a}p + \frac{C_{n_r}b}{2V_a}r + C_{n_{\delta_a}}\delta_a + C_{n_{\delta_r}}\delta_r\right] \quad [2.19]$$

The propulsive force for a normally configured aircraft acts along the x_b axis. The following general equation represents the propulsive force:

$$f_p = \frac{1}{2}\rho S_{prop} C_{prop} \begin{bmatrix} (k_{motor}\delta_t)^2 - V_a^2 \\ 0 \\ 0 \end{bmatrix} \quad [2.20]$$

The model for thrust used in this study was not calculated in this way. The motor was placed on an engine stand and the thrust was measured as a function of throttle percentage. The thrust needed in flight can be calculated and supplied as a throttle percentage input. The model that was determined on the test stand is presented in equation 2.21.

$$T = 5\delta_t^2 + 0.24\delta_t + 0.24 \quad [2.21]$$

This relationship describes the thrust output in pound force to throttle position in percent. Multiple thrust tests have been performed for the electric motor on the DG808S. A comparison of a more recent test is presented in figure 3.

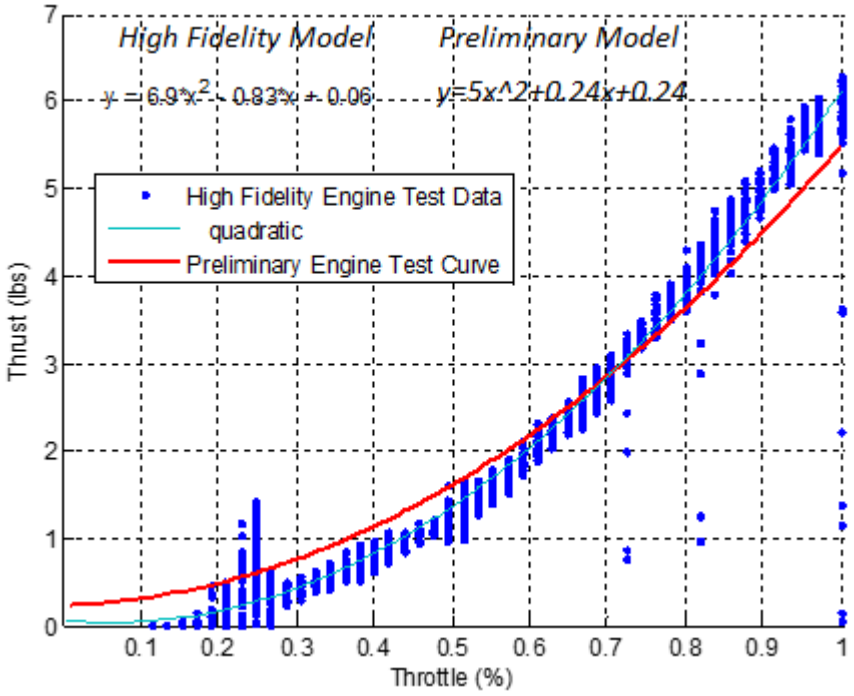

Figure 3: Comparison of High Fidelity Engine Model with Preliminary Model

The preliminary engine model does not align with the more recently obtained high fidelity model on both low and high end RPM. The controller in this research has not been updated to the high fidelity engine model, however since this is a general concept and the DG808S and NMPC are used strictly as a means of presenting the concept. The integrity of this work is not lost. The newer model will be updated in the near future.

A moment is also associated with all rotating engines. A torque due to the reactive force of the motor induces a roll motion represented by the following:

$$m_p = \begin{bmatrix} -k_{T_p}(k_\omega \delta_t)^2 \\ 0 \\ 0 \end{bmatrix} \quad [2.22]$$

For this aircraft, because of the relatively low torque, light weight of the propeller and large I_{xx}, this moments is assumed to be zero and any roll motion will be easily compensated by the lateral controller. However, because of the geometry of this aircraft, a different propulsive moment should be taken into account. The motor is mounted nine inches above the x_b axis. This induces a pitching moment when thrust is applied. This moment is represented by the following:

$$M_T = r\delta_t \quad [2.23]$$

Where r is the distance from the x_b axis to the center of thrust and δ_t is the change in thrust. For the DG808S the distance r is 8 inches and produces a relatively large negative pitching moment. This must be taken into account in the dynamic modelling of the aircraft.

2.3 Aircraft Kinematics and Dynamics

The following four sets of equations represent the states used in the 6 degree of freedom (DoF) model. The kinematics are represented by the following equations:

$$\begin{bmatrix}\dot{p_n}\\ \dot{P_e}\\ \dot{P_d}\end{bmatrix} = R_b^I \begin{bmatrix}u\\ v\\ w\end{bmatrix} + \begin{bmatrix}w_N\\ w_E\\ w_D\end{bmatrix} \quad [2.24]$$

$$\begin{bmatrix}\dot{\phi}\\ \dot{\theta}\\ \dot{\psi}\end{bmatrix} = \begin{bmatrix}1 & sin\phi tan\theta & cos\phi tan\theta\\ 0 & cos\phi & -sin\phi\\ 0 & \frac{sin\phi}{cos\theta} & \frac{cos\phi}{cos\theta}\end{bmatrix}\begin{bmatrix}p\\ q\\ r\end{bmatrix} \quad [2.25]$$

The dynamics are represented by the following equations:

$$\begin{bmatrix}\dot{u}\\ \dot{v}\\ \dot{w}\end{bmatrix} = \begin{bmatrix}rv - qw\\ pw - ru\\ qu - pv\end{bmatrix} - \frac{1}{m}\begin{bmatrix}f_x\\ f_y\\ f_z\end{bmatrix} \quad [2.26]$$

$$f_x = -f_{drag} \quad [2.27]$$

$$f_z = -f_{lift} \quad [2.28]$$

$$\begin{bmatrix}\dot{p}\\ \dot{q}\\ \dot{r}\end{bmatrix} = \begin{bmatrix}\Gamma_1 pq - \Gamma_2 qr\\ \Gamma_5 pr - \Gamma_6(p^2 - r^2)\\ \Gamma_7 p - \Gamma_1 qr\end{bmatrix} + \begin{bmatrix}\Gamma_3 l + \Gamma_4 n\\ \frac{1}{J_y}m\\ \Gamma_4 l + \Gamma_8 n\end{bmatrix} \quad [2.29]$$

Where the moment of inertia are included in the following relationships:

$$\Gamma = J_x J_y - J_{xz}^2 \quad [2.30]$$

$$\Gamma_1 = \frac{J_{xz}(J_x - J_y + J_z)}{\Gamma} \quad [2.31]$$

$$\Gamma_2 = \frac{J_z(J_z - J_y) + J_{xz}^2}{\Gamma} \quad [2.32]$$

$$\Gamma_3 = \frac{J_z}{\Gamma} \quad [2.33]$$

$$\Gamma_4 = \frac{J_{xz}}{\Gamma} \quad [2.34]$$

$$\Gamma_5 = \frac{J_z - J_x}{J_y} \quad [2.35]$$

$$\Gamma_6 = \frac{J_{xz}}{J_y} \quad [2.36]$$

$$\Gamma_7 = \frac{(J_x - J_y)J_x + J_{xz}^2}{\Gamma} \quad [2.37]$$

$$\Gamma_8 = \frac{J_x}{\Gamma} \quad [2.38]$$

2.4 DG808S Geometry and Dynamic Modeling

The DG808S electric glider is a 13 foot wingspan scale model of the DG-Flugzeugbau DG808S. This scale model aircraft with all avionics is 9.7 pounds with a trim speed of 35 knots. This aircraft has an in-line landing gear configuration and a relatively large wingspan. The large wingspan and low weight make it susceptible to high wind and gusty conditions. Since this aircraft is used for multiple research purposes including dynamic soring and swarm flight, trajectory following must be performed as accurately as possible. Using a controller like the NMPC this means that the dynamic model must be as accurate as possible.

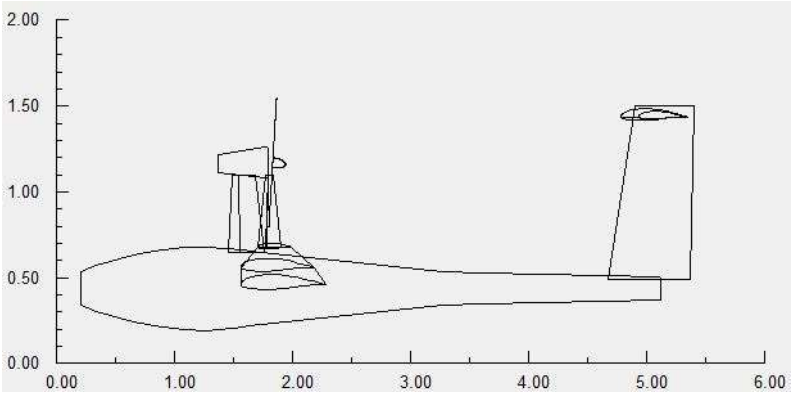

Figure 4: Advanced Aircraft Analysis Side view of the DG808S [37]

The longitudinal and lateral directional modes are determined using Advanced Aircraft Analysis (AAA). AAA is an aircraft design, stability and control software developed by DARCorp. AAA uses detailed information of the aircraft and calculates weight and balance, aerodynamics, stability and control and performs trim and flying quality analysis [38].

The onboard controller must have an accurate dynamic model to generate the expected real time behavior. In order to accomplish this a complete understanding of the aircraft dynamic characteristics are necessary prior to flight. The aileron, elevator and rudder are restricted to 20° maximum deflection. The stability and control derivatives are presented in tables 1 and 2.

The control derivatives are presented in radian per second. The flight characteristics are presented in tables 2 and 3.

Table 1: Longitudinal Stability and Control Derivatives

C_{L_0}	0.351	C_{D_0}	0.021	C_{m_0}	0.039
C_{L_α}	8.405	C_{D_α}	0.100	C_{m_α}	-0.629
C_{L_q}	6.549	C_{D_q}	0.000	C_{m_q}	-23.41
$C_{L_{\delta_e}}$	0.083	$C_{D_{\delta_e}}$	0.004	$C_{m\,\delta_e}$	-0.442

Table 2: Lateral Directional Stability and Control Derivatives

C_{Y_β}	-0.2746	C_{l_β}	-0.0459	C_{n_β}	0.0586
C_{Y_p}	0.0904	C_{l_p}	-0.8652	C_{n_p}	-0.0490
C_{Y_r}	0.1239	C_{l_r}	0.0851	C_{n_r}	-0.0355
$C_{Y_{\delta_a}}$	0.0000	$C_{l_{\delta_a}}$	0.6013	$C_{n_{\delta_a}}$	-0.0302
$C_{Y_{\delta_r}}$	0.1396	$C_{l_{\delta_r}}$	0.0041	$C_{n_{\delta_r}}$	-0.0383

Table 3: DG808S Longitudinal Modes

Phugoid		Short Period	
Frequency	Damping Ratio	Frequency	Damping Ratio
0.84	0.08	NA	NA

Table 4: DG808S Lateral Directional Modes

Roll	Spiral	Dutch Roll	
Time Constant	Time Constant	Frequency	Damping Ratio
0.84	-30.6	4.25	0.20

The attitude of the aircraft must also be limited upon landing. For the DG808S the most ideal landing should be performed with the x_b aligned with the runway and the roll angle less than 5°as is presented in figure 5.

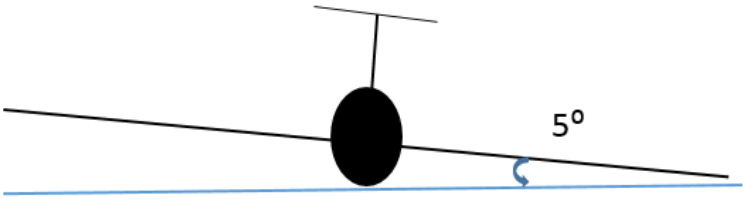

Figure 5: Front View of DG808S with Landing Bank Angle Limitation

Upon landing, the DG808S wingspan limits the roll angle to five degrees. Anything beyond five degrees will result in a wing tip strike on the ground. Since the roll angle is limited this results in a crab angle being used to maintain the appropriate heading parallel to the runway. A zero sideslip, full rudder compensation can be used for flight of this aircraft. However, upon landing in crosswind, this would result in the aircraft attitude being at a crab angle. Since this aircraft has an in-line landing gear configuration the wheels should touchdown simultaneously. If the aircraft lands at a large enough crab angle it could result in a ground roll possibly damaging the aircraft. Reducing, if not eliminating, this angle will reduce this risk. Combining the roll and crab will increase the crosswind landing envelope.

Chapter 3

Landing in Crosswind

This chapter defines crosswind and describes the techniques used for landing. Section 3.1 defines crosswind and the challenges it creates. Section 3.2 describes the typical lateral and directional techniques used for landing in crosswind. Section 3.2 describes the longitudinal landing techniques.

3.1 Wind

Wind is spatial and temporal which makes predicting its behavior extremely difficult. Due to the risk involved with crosswind landings it is paramount that it be understood and mitigated.

Landing in crosswind increases the complexity for a pilot, which leads to increased risk [1].

- Thirty three percent of aircraft accidents at landing are directly due to adverse wind conditions [1].
- Runway condition and crosswind is a factor in 70% of runway excursion events [1].
- 85% of crosswind accidents occur at landing [1].

Given these statistics it is clear that landing techniques that compensate for crosswind effects are important. These techniques are in widespread use in manned flight, but have yet to be implemented in regular unmanned flight. The heightened affects for lightweight UAS increases the importance of employing these techniques and finding an automatic landing sequence that reduces the risk to these aircraft as well as the ground crew. Before combating these effects crosswind and the terms used are first defined. A crosswind description is presented in figure 6 for a crabbed landing approach.

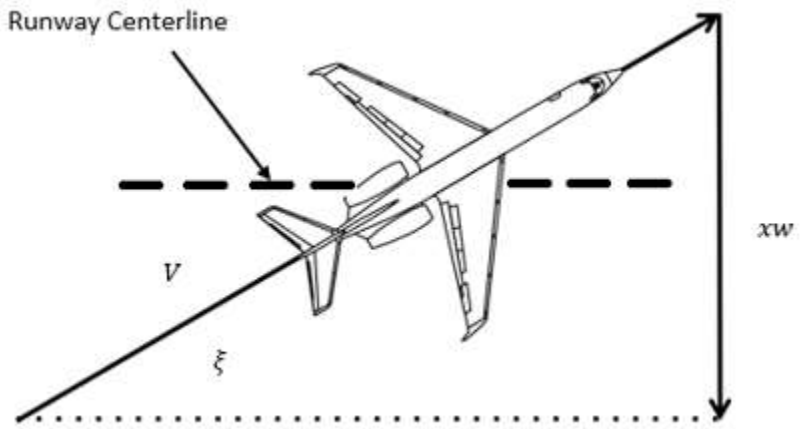

Figure 6: Crosswind Component and Aircraft in Crab Landing Attitude [39]

In figure 6 the crosswind component is impacting port side of the aircraft. This forces the aircraft to angle nose into the wind to maintain heading along the runway centerline. Upon approach and landing this angle is referred to as the crab angle ξ.

$$\xi = \sin^{-1}\frac{xw}{V} \qquad [3.1]$$

The crosswind at cruise altitude may be higher than at ground level. Due to the growing demand to reduce the use of fossil fuels, wind research has become popular. The use of wind turbines for energy production has become widespread and wind research can help find more efficient processes. Wind as a function of height has been researched to find the best height and environments for wind turbines. This also affects the landing of aircraft at airports in large cities or the countryside. Wind as a function of height is presented in figure 7.

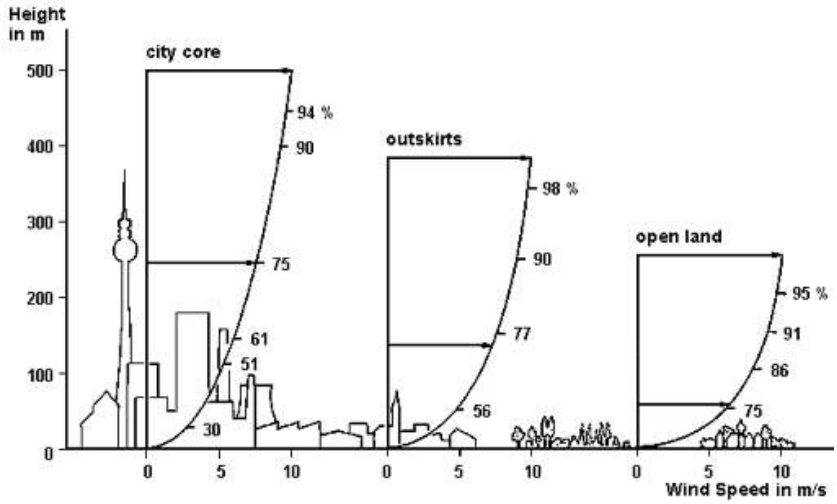

Figure 7: Wind Speed as a Function of Height [40]

As seen in figure 7, not only is the wind a function of height but is also impacted by ground objects such as buildings and trees. This will all have an effect on the landing performance of the aircraft and should always be considered.

3.2 Crosswind Landing Techniques

There are several crosswind landing techniques in use today. The sideslip technique allows the airplane to land in line with the runway. The ailerons and rudder are used to keep the x_b axis aligned with the centerline of the runway upon approach and landing. This is a good technique for UAS landings when there is wing tip clearance and the aircraft is a tricycle style. However, the roll angle is limited by the wingspan and the placement of the wings on the fuselage, as well as the dihedral, so this may only be possible in low crosswind conditions or when the geometry of the aircraft allows for a relatively large roll angle upon landing.

Another useful technique is the crab landing orientation. This technique allows the aircraft to maintain wings level flight, however the aircraft x_b axis is not aligned with the runway. The aircraft either corrects the attitude to align immediately before landing or, in the case of a tricycle style aircraft when a slight roll is used, the alignment can occur after the main gear has

touched down. The up wind wheel will touch down first allowing the pilot to align the aircraft while the other wheels contact.

These landing styles are limited for an in-line landing gear configured aircraft. The sideslip landing is the best approach. If the wingspan of the aircraft is large then this will limit the roll that is necessary to counteract the crosswind so the overall crosswind landing for the aircraft is limited. This is the case for the DG808S. A possible solution is that the aircraft can change attitude directly before landing. This is a viable option since the wind gradient should decrease at low altitudes [12, 14].

This characteristic can be exploited for small UAS's. Since these aircraft are so close to the ground on landing, and in particular the DG808S has small landing gear, it can be assumed that the crosswind at touchdown will affect the aircraft minimally. Because of this result either landing mode can be used. Since the roll angle will allow the aircraft trajectory to maintain better alignment with the runway, thus bringing in a factor of safety on rollout, the sideslip command will be implemented on landing. This will ensure that a "best" condition for landing is maintained while providing a safe rollout.

However, in the case that the winds are high just before landing this may cause landing at an angle since the wind could blow the aircraft off course. Due to these affects the crosswind techniques must be implemented. The sideslip and crab landing techniques are presented in figures 8 and 9. A combined crab and sideslip technique is presented in figure 10.

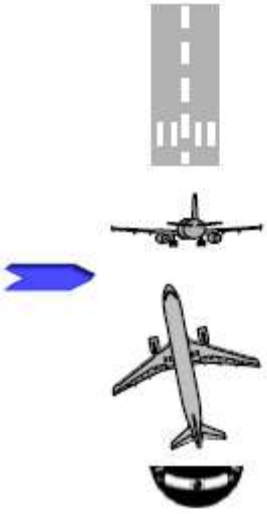

Figure 8: Crab Landing (41)

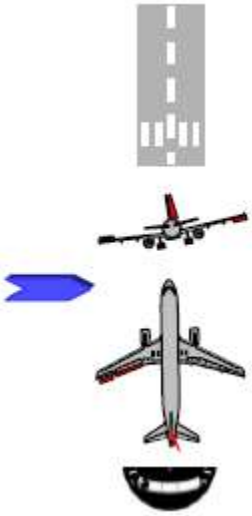

Figure 9: Sideslip Landing (41)

Figure 10: Combination Crab and Sideslip (42)

During the sideslip landing technique the aircraft must stay below the maximum bank angle for landing while maintaining the required crab angle to remain aligned with the runway. As long as the crosswind magnitude allows the aircraft to stay in the sideslip mode then this is the technique that will be used. If a crab motion must be employed then the maximum landing bank angle will be set and the crab technique will be employed. This will allow the aircraft to expand the flight envelope for this phase of flight. Experimental testing must be performed to determine the maximum safe crab angle upon landing for a given aircraft.

For an airplane under NMPC autopilot control, when a zero sideslip is commanded without wind simulation then the aircraft lines up with the trajectory causing a crab approach. Using the ailerons and rudder to compensate for the crosswind could increase risk for a small UAS with a large wingspan like the DG808S. When the wind is high enough the bank angle will be steep and cause a tip strike on the runway. In this case the crab method must be employed. Also, in high wind conditions this can be used to slow the aircraft ground speed and use crab simultaneously to land at a low speed.

Rollout is the most important part of a crosswind landing since this is where most accidents happen [10]. The controller should be ongoing for rollout while the velocity is reduced to zero. No other changes should be made as the aircraft should remain on course under the same conditions. It is important that the controller performance not be diminished by the introduction of the lateral guidance.

This work presents one method in two flight phases that both improves trajectory tracking in the cruise phase and increases the flight envelope of the landing phase. When an attitude is commanded, with loss of controller support, before touchdown the aircraft is susceptible to changing wind conditions and uncertainty. With this method the controller is still allowed to react to the wind throughout the landing phase reducing uncertainty. During this phase the aircraft is allowed to hold an optimal roll angle thus reducing the crab angle of the aircraft upon landing. This is performed by commanding an optimal sideslip based on the estimated crosswind and geometry. During the coordinated turn the aircraft remains below the performance and geometric constraints while remaining in control of the aircraft allowing for a safe and controlled landing.

3.3 Longitudinal Landing Guidance

The landing sequence is determined using FAR 23 requirements. The FAA stipulates that the landing approach speed be a minimum of $1.3V_{stall}$ and the glide slope be maximum with engine out and minimum drag setting for a single engine prop [43]. This requirement is met setting the aircraft total airspeed to $1.3V_{stall}$. Due to lack of an accurate low speed model for this aircraft, the DG808S model is generated at 35 Knots. This is higher than $1.3V_{stall}$ but since the procedure outlined for the landing sequence is generic, it can be applied to any aircraft at any speed. The determination of the landing sequence is outlined below [44]. The aircraft flight path is presented in figure 11. The landing requirements for transport aircraft as specified by the FAA and JAA are presented in figure 12.

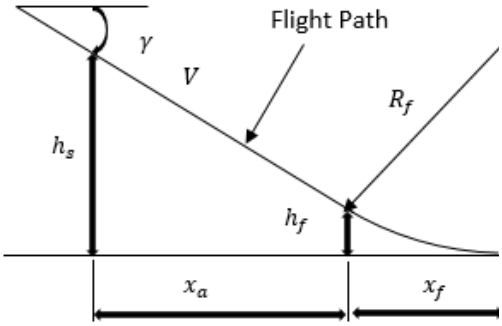

Figure 11: Approach and Flare for Longitudinal Landing Planning (44)

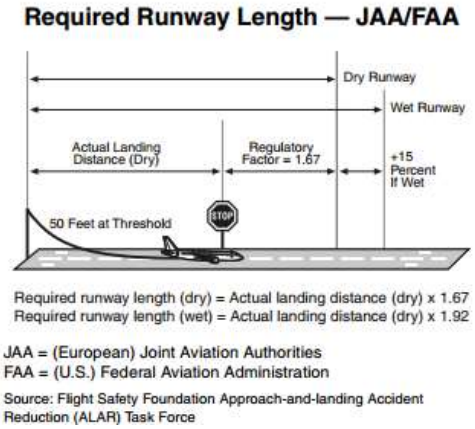

Figure 12: Landing Requirements for Transport Aircraft by JAA and FAA (45)

The approach and flare trajectory is shown in figure 10. The screen height h_s is a height of 50 feet that the aircraft must clear upon approach while still maintaining the ability to stop on the runway as designated by the FAA [43]. As this simulation is a proof of concept rather than a flight plan prior to testing this regulation is not considered. The distance x_a is the approach

distance and is the portion of flight where the aircraft is approaching at the glide path angle γ. The approach distance and time is developed in equations 3.2 through 3.5.

$$x_a = \frac{h_s - h_f}{\tan\gamma} \quad [3.2]$$

The approach airspeed is constant. This leads to the following equation for the time for the approach leg:

$$t_a = \frac{x_a}{V_a \cos\gamma} \quad [3.3]$$

The approach velocity is approximately $1.3V_{stall}$ where V_{stall} is represented in equation 3.4.

$$V_{stall} = \sqrt{\frac{2\left(\frac{W}{s}\right)}{\rho C_{L_a}}} \quad [3.4]$$

The flare stage is determined by the controller functionality and must be set by simulation. Equation # is used as the trajectory while the constant τ describes an acceptable curvature (17).

$$h_{flare} = h_{0_{flare}} e^{-t/\tau} \quad [3.5]$$

After running simulations to determine how the aircraft would react under these conditions the most suitable values for $h_{0_{flare}}$ and τ are 52 feet and 565.

Chapter 4

Nonlinear Model Predictive Control

This section outlines the control implementation used in this study. Section 4.1 outlines the guidance, section 4.2 outlines navigation and section 4.3 outlines control. The method for attitude control used in this research may be applied to any guidance that does not directly assign an attitude based on crosswind estimation. The controller used here is the nonlinear model predictive controller (NMPC) with moving waypoint guidance. A more detailed formulation for the moving point guidance and NMPC control is presented in [13].

4.1 Moving Waypoint Guidance

The guidance model incorporates moving waypoints. Rather than using singular points in space as the target the moving waypoint method generates new points each time step. As the aircraft moves new waypoints are generated further along the segment $\boldsymbol{a}, \boldsymbol{b}$ causing a velocity generation in the aircraft to follow the points. The NMPC uses lateral and longitudinal error angles to track the trajectory and reduce overshoot. The line segment $\boldsymbol{a}$, $\boldsymbol{b}$ represents the current segment of the trajectory of the reference flight guidance. The point ***d*** is located perpendicular to the aircraft along the defined segment. The point ***r*** is located a specified distance in front of ***d*** along the segment. While ***d*** is moving, ***r*** moves along the segment staying the same distance in front. The point ***p*** is defined as the position of the aircraft and the vector $\vec{V}$

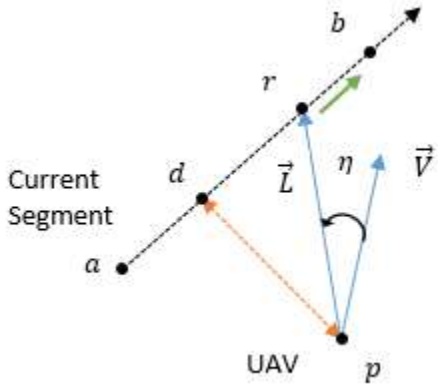

Figure 13: Geometry of the Guidance Law

is the inertial velocity vector. The vector $\vec{L}$ is defined from ***p*** to ***r***. It can be seen that as the distance ***pd*** decreases to zero the cross track error η also decreases to zero. This angle is then projected into two components η_{lon} and η_{lat}.

The point ***d*** is calculated as follows:

$$d(t) = \begin{bmatrix} d_N(t) \\ d_E(t) \\ d_H(t) \end{bmatrix} = a(t) + q(t)[b(t) - d(t)] \quad [4.1]$$

$$q(t) = \frac{[p(t)-a(t)]\cdot[b(t)-a(t)]}{|b(t)-a(t)|^2} \quad [4.2]$$

The symbol $|\cdot|$ represents the distance between two points. Points ***a*** and ***b*** are constant unless the line segment is changed. The point ***r*** is located at a fixed distance and is defined by the following:

$$r(t) = \begin{bmatrix} r_N(t) \\ r_E(t) \\ r_H(t) \end{bmatrix} = d(t) + m(t)[b(t) - d(t)] \quad [4.3]$$

$$m(t) = \frac{|r(t)-d(t)|}{|b(t)-d(t)|} \quad [4.4]$$

The distance $|r(t) - d(t)|$ is fixed and the point ***r***, always moving to the right, is a target for the aircraft.

$$L(t) = r(t) - p(t) = \begin{bmatrix} r_N(t) - p_N(t) \\ r_E(t) - p_E(t) \\ r_H(t) - p_H(t) \end{bmatrix} \quad [4.5]$$

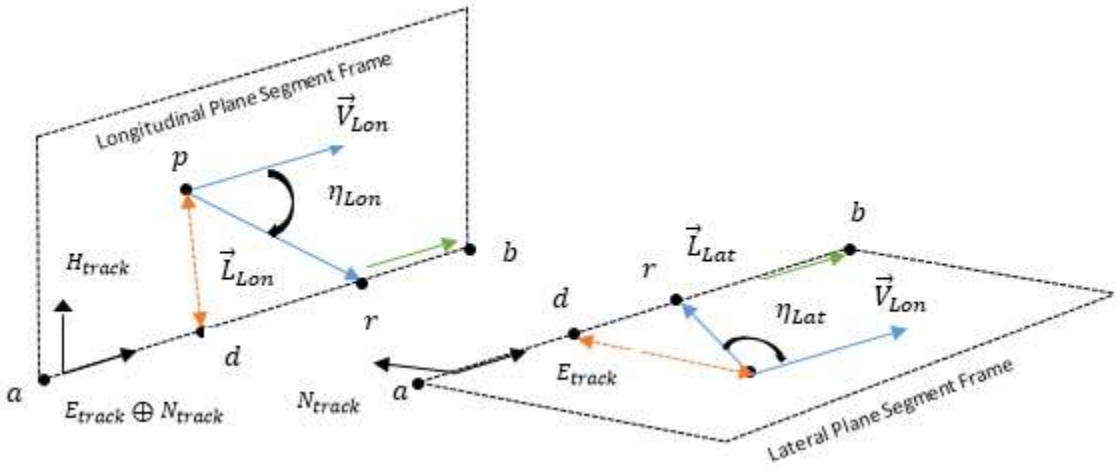

Figure 14: Lateral and Longitudinal Plane Segments

$$\vec{L}(t) = r(t) - p(t) = \begin{bmatrix} r_N(t) - p_N(t) \\ r_E(t) - p_E(t) \\ r_H(t) - p_H(t) \end{bmatrix} \quad [4.6]$$

In order to define the vectors $\vec{V}$ and $\vec{L}$ a rotation from the inertial frame to the segment frame is performed.

$$R_I^s = R_w^{b\,T} \quad [4.7]$$

The angles used are α_{track} and β_{track}. The angles' geometric representation is presented in figure 15.

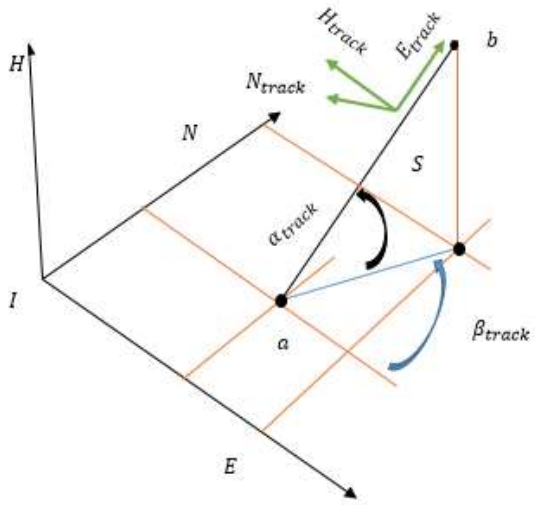

Figure 15: Segment Rotations

The conversion from the inertial frame to the segment frame is needed to get both η_{Lat} and η_{Lon}. $\vec{V}$ and $\vec{L}$ undergo this transformation. The transformation matrix is represented in equation 4.8.

$$C_I^S = \begin{bmatrix} \cos\alpha_{track}\cos\beta_{track} & \sin\beta_{track} & \sin\alpha_{track}\cos\beta_{track} \\ -\cos\alpha_{track}\sin\beta_{track} & \cos\beta_{track} & -\sin\alpha_{track}\sin\beta_{track} \\ -\sin\alpha_{track} & 0 & \cos\alpha_{track} \end{bmatrix} \quad [4.8]$$

The update vectors are presented in equations 4.9 and 4.10.

$$\vec{V}_{track}(t) = \begin{bmatrix} \dot{p}_{N\,track}(t) \\ \dot{p}_{E\,track}(t) \\ \dot{p}_{H\,track}(t) \end{bmatrix} \quad [4.9]$$

$$\vec{L}_{track}(t) = \begin{bmatrix} [r_N(t) - p_N(t)]_{track} \\ [r_E(t) - p_E(t)]_{track} \\ [r_H(t) - p_H(t)]_{track} \end{bmatrix} \quad [4.10]$$

Breaking down into lateral and longitudinal planes η_{lat} and η_{lon} the definitions are presented below.

$$\eta_{lat}(t) = arctan\left(\frac{[r_N(t)-p_N(t)]_{track}}{[r_E(t)-p_E(t)]_{track}}\right) - arctan\left(\frac{\dot{p}_{N\,track}}{\dot{p}_{E\,track}}\right) \quad [4.11]$$

$$\eta_{lon}(t) = arctan\left(\frac{[r_H(t)-p_H(t)]_{track}}{[r_E(t)-p_E(t)]_{track}\oplus[r_N(t)-p_N(t)]_{track}}\right) - arctan\left(\frac{\dot{p}_{H_{track}}}{\dot{p}_{E_{track}}\oplus\dot{p}_{N_{track}}}\right) \quad [4.12]$$

Where

$$x\oplus y = \sqrt{x^2+y^2} \quad [4.13]$$

The states presented used for this model are presented in equation 4.14.

$$x^T = \{U, V, W, \phi, \theta, \psi, P, Q, R, p_N, p_E, p_H, \eta_{Lat}, \eta_{Lon}\} \quad [4.14]$$

4.2 NMPC Control

The general NMPC formulation can be found in (13, 46, 47). The receding horizon problem is formulated by the following:

$$P_N = \min_u\{V(x,u)\} \quad [4.15]$$

With the cost function presented in equation 4.16.

$$V(x_0,u) = \sum_{k=1}^{N} l(x_{k+1},u_k) \quad [4.16]$$

$$l(x_{k+1},u_k) = x_{k+1}^T Q_{k+1} x_{k+1} + u_k^T R_k u_k \quad [4.17]$$

Where $x_k \in R^n$ and $u_k \in R^m$ are state and control vectors respectively. The following constraints must be satisfied:

$$u_k \in U \quad [4.18]$$

$$x_k \in X \quad [4.19]$$

Where U is a convex, compact subset of R^m, and X is a convex, closed subset of R^n. The constraints are determined by the size and rate of change of the signals, and the minimum and

maximum limits of the dynamics of the real system. A numerical search algorithm finds the best values for the control $u = \{u_1, u_2, \dots, u_N\}$ that minimizes the cost function $V(x, u)$.

$$x_1 = f_d(x_0, u_0) \quad [4.20]$$

$$x_2 = f_d(x_1, u_1) \quad [4.21]$$

$$\vdots$$

$$x_N = f_d(x_{N-1}, u_{N-1}) \quad [4.22]$$

$$x_{N+1} = f_d(x_N, u_N) \quad [4.23]$$

Combining the equations gives

$$x_{N+1} = f_d(f_d(\dots(f_d(x_0, u_0), u_1) \dots, u_{N-1}), u_N) \quad [4.24]$$

The receding horizon expression is dependent on x_0, u_0.

The solution to this problem is a numerical method called Sequential Quadratic Programming (SQP).

$$\begin{bmatrix} u^{i+1} \\ \lambda^{i+1} \end{bmatrix}_{(mN+p)\times 1} = \begin{bmatrix} u^{i} \\ \lambda^{i} \end{bmatrix}_{(mN+p)\times 1} + \begin{bmatrix} \Delta u^{i} \\ \Delta \lambda^{i} \end{bmatrix}_{(mN+p)\times 1} \quad [4.25]$$

$$\begin{bmatrix} \Delta_{uu}^2 V & -A^T \\ A & 0 \end{bmatrix}_{(mN+p)\times(mN+p)} \begin{bmatrix} \Delta u^{i} \\ \Delta \lambda^{i} \end{bmatrix}_{((mN+p)\times 1} = \begin{bmatrix} -\Delta_u V + A^T \lambda \\ c \end{bmatrix}_{(mN+p)\times 1} \quad [4.26]$$

$$A^T(u) = \left[\Delta_{c_1}(u) \ \dots \ \Delta c_P(u)\right] \quad [4.27]$$

$$V(u) = e^T(u) e(u) \quad [4.28]$$

$$e(u) = \begin{bmatrix} Q_2^{\frac{1}{2}} x_2 \\ \vdots \\ Q_{N+1}^{\frac{1}{2}} x_{N+1} \\ R_1^{\frac{1}{2}} u_1 \\ \vdots \\ R_1^{\frac{1}{2}} u_2 \end{bmatrix}_{(mN+mN)\times 1} \quad [4.29]$$

$$e(u + \Delta u) \approx e(u) + J(u)\Delta u \quad [4.30]$$

$$J(u) = \begin{bmatrix} Q_2^{\frac{1}{2}} \frac{\delta x_2}{\delta u_1^T} & 0 & 0 & \dots & 0 \\ Q_2^{\frac{1}{2}} \frac{\delta x_2}{\delta u_1^T} & Q_2^{\frac{1}{2}} \frac{\delta x_2}{\delta u_1^T} & 0 & \dots & 0 \\ \vdots & \vdots & \vdots & \ddots & 0 \\ Q_2^{\frac{1}{2}} \frac{\delta x_2}{\delta u_1^T} & Q_2^{\frac{1}{2}} \frac{\delta x_2}{\delta u_1^T} & Q_2^{\frac{1}{2}} \frac{\delta x_2}{\delta u_1^T} & \dots & Q_2^{\frac{1}{2}} \frac{\delta x_2}{\delta u_1^T} \\ R_1^{1/2} & 0 & 0 & \dots & 0 \\ 0 & R_1^{1/2} & 0 & \dots & 0 \\ 0 & 0 & R_1^{1/2} & \dots & 0 \\ \vdots & \vdots & \vdots & \ddots & 0 \\ 0 & 0 & 0 & \dots & R_1^{1/2} \end{bmatrix} \quad [4.31]$$

$$V(u + \Delta u) = (e(u) + J(u)\Delta u)^T (e(u) + J(u)\Delta u)$$

$$= e^T(u)e(u) + 2\Delta u^T J(u)^T e(u) + \Delta u^T J^T(u) J(u)\Delta u \quad [4.32]$$

The gradient and Hessian can be obtained by forming the error vector $e(u)$ and the Jacobian $J^T(u)$ when looking at equation 4.32 as the second order Taylor expansion of the cost function $V(u)$.

Chapter 5

Wind Estimation Validation and Extended Kalman Filter

The airspeed is measured directly using an onboard pitot tube. The pitot tube measures the wind directly along the aircraft x_b. A sideslip angle may also occur where the aircraft attitude is adjusted so the wind axis and the stability axis are not aligned. The airspeed components along the y and z axis are not measured. A wind estimation extended Kalman filter is implemented. In this model the acceleration is used and a full nonlinear simulation is run to estimate the 3 dimensional wind components. The full equation representing the total body fixed velocity were presented in section 2.1. The body calculated velocity and acceleration components are presented in equations 5.1 and 5.3.

$$\begin{bmatrix} u \\ v \\ w \end{bmatrix} = \begin{bmatrix} V_A cos\alpha cos\beta \\ V_A sin\beta \\ V_A sin\alpha cos\beta \end{bmatrix} \quad [5.1]$$

This gives an alternate means than the measured accelerations from the on board IMU. Since the wind cannot be directly measured, it is calculated through the follow equations [12]:

$$\omega_i = V_I - R_b^I V_b \quad [5.2]$$

$$\begin{bmatrix} \dot{\omega}_{xb} \\ \dot{\omega}_{yb} \\ \dot{\omega}_{zb} \end{bmatrix} = \begin{bmatrix} a_{xb} - q\omega + rv - gsin\theta - \dot{u} \\ a_{yb} - ru + p\omega + gcos\theta sin\phi - \dot{v} \\ a_{zb} - pv + qu + gcos\theta cos\phi - b_{imu_z} - \dot{\omega} \end{bmatrix} \quad [5.3]$$

Equation 5.2 is used in the physics based model to calculate the next step component of wind velocity. Equation 5.3 calculates the wind acceleration using inertial measurements and should be more accurate [12]. The estimated wind is updated each time step using the acceleration and equation 5.2 is the modeled wind. For the simulation when the true wind speed

is known the error between the physics based model and the true wind value with included noise is then compared in plots. For this simulation a full nonlinear formulation is used and the states are presented in 5.4.

$$\dot{\boldsymbol{x}} = \begin{bmatrix} \dot{P}_n \\ \dot{P}_e \\ \dot{P}_d \\ \dot{\omega}_n \\ \dot{\omega}_e \\ \dot{\omega}_d \\ \dot{\phi} \\ \dot{\theta} \\ \dot{\psi} \\ \dot{p} \\ \dot{q} \\ \dot{r} \\ \dot{\alpha} \\ \dot{\beta} \\ \delta_T \\ \delta_E \\ \delta_A \\ \delta_R \end{bmatrix} = \begin{bmatrix} ucos\phi cos\psi + v(-cos\phi sin\psi + sin\phi sin\theta cos\phi) + w(sin\phi sin\psi + cos\phi sin\theta cos\psi - \omega_n \\ ucos\theta sin\psi + v(cos\phi cos\psi + sin\phi sin\theta sin\psi) + w(-sin\phi cos\psi + cos\phi sin\theta sin\psi) - \omega_e \\ usin\theta - vsin\phi cos\theta - wcos\phi cos\theta - \omega_n \\ R^i_{b_x}\dot{\omega}_{x_b} \\ R^i_{b_y}\dot{\omega}_{y_b} \\ R^i_{b_z}\dot{\omega}_{z_b} \\ p + tan\theta(qsin\phi + rcos\phi) \\ qcos\phi - rsin\phi \\ (qsin\phi + rcos\phi)/cos\theta \\ (I_{xz}[I_x - I_y + I_z]pq - [I_z(I_z - I_y) + I^2_{zx}]qr + I_z L_A + I_{xz}N_A)/(I_x I_z - I^2_{xz}) \\ ([I_z - I_x]pr - I_{xz}[p^2 - r^2] + M_A)/(I_x I_z - I^2_{xz}) \\ ([I_x - I_y)I_x + I^2_{xz}]pq - I_{xz}[I_x - I_y + I_z]qr + I_{xz}L_A + I_x N_A)/(I_x I_z - I^2_{xz}) \\ (u\dot{w} - w\dot{u})/(uu + ww) \\ (V_t\dot{V} - V\dot{V}_t)/(V_t^2 \cos\beta) \\ (\delta_{T_{CMD}} - \delta_T)/\tau_T \\ (\delta_{E_{CMD}} - \delta_E)/\tau_E \\ (\delta_{A_{CMD}} - \delta_A)/\tau_A \\ (\delta_{R_{CMD}} - \delta_R)/\tau_R \end{bmatrix} \quad [5.4]$$

To reduce the error in estimating the wind an extended Kalman filter is used. The filter reduces the error of the measurements and the physics based model by using the weighted least squares method. The formulation for the extended Kalman filter is presented below. The simulation is discrete therefore a calculation is performed for each time step. The time update is performed for the calculation.

$$\boldsymbol{x}[k] = \boldsymbol{x}[k-1] + \Delta t \dot{\boldsymbol{x}}[k-1] \quad [5.5]$$

The measurement and calculated data is used for the following general extended Kalman filter method.

$$A = \frac{\delta F}{\delta \boldsymbol{x}},\ H = \frac{\delta G}{\delta \boldsymbol{x}} \quad [5.6]$$

The A matrix is the state Jacobian and the H matrix is the measurement Jacobian. The initial step is to predict the next state and covariance.

$$\hat{\boldsymbol{x}}[k] = A\boldsymbol{x}[k-1] \quad [5.7]$$

$$\bar{P}k[k] = APk[k-1]A' + Q \quad [5.8]$$

The next step is to update the state and covariance with the Kalman gain and measurement residuals.

$$K[k] = \bar{P}k[k]H'/(H\bar{P}k[k]H' + R) \quad [5.9]$$

$$\boldsymbol{x}[k] = \hat{\boldsymbol{x}}[k] + K[k](\boldsymbol{y}[k] - H\hat{\boldsymbol{x}}[k]) \quad [5.10]$$

$$Pk[k] = \bar{P}k[k] - K[k]H\bar{P}k[k] \quad [5.11]$$

The procedure is repeated for each measurement and time update.

Chapter 6

Attitude Based Crosswind Rejection

In this section lateral directional attitude guidance based on crosswind component is defined. With an accurate estimation of crosswind, an attitude for the aircraft can be commanded that simultaneously reduces the time to trajectory convergence and increases the trajectory tracking. By utilizing the crosswind estimation a known disturbance is rejected by forcing the aircraft into a coordinated turn into the crosswind rather than just relying on the deviation from the prescribed path. Specifically for this NMPC control, a roll angle is commanded by creating a sideslip based on crosswind component magnitude. The command input is presented in equation 6.1 and was developed in section 2.1.

$$\beta_{cmd} = -K_{\beta} \sin \frac{v}{\sqrt{u^2+v^2+w^2}} \qquad [6.1]$$

This is calculated in the guidance module of the NMPC, therefore rather than the sideslip angle being a measured term based on aircraft attitude and wind it is a reactive term input into the system prior to controlling the dynamics.

Chapter 7

Results and Discussion

This section presents the results for longitudinal landing calculations, wind estimation and lateral and longitudinal simulations for the cruise and landing phases of the DG808S. K_β is implemented in both landing and cruise phases and optimal values for landing are developed.

7.1 Landing Conditions for the DG808S

This section defines the landing parameters for the DG808S. The results presented are the ideal landing conditions based on the regulations defined in section 2. The calculated landing conditions are presented in table 5.

Table 5: Landing Parameters for the DG808S

γ (deg)	$x_a\ (ft)$	$h\ (ft)$	$RD\ (ft)$	t (sec)
-3.98	2650	200	4.25	47

7.2 Wind Estimation Results

Similar to the landing and cruise simulations, the wind estimation simulation is run with east crosswind. In the simulation the known ground truth wind is provided with random error of 0 mean and a variance of 0.144 fps. The extended Kalman filter, as defined in chapter 5 is used to estimate the wind. A comparison of ground truth wind and wind estimation is presented in figures 16, 17 and 19 and the performance measure covariance trace is presented in figure 18. The step input is shown from the mid-range of the simulation when the filter has converged and the aircraft has converged on the desired path. The validation is performed by combining the wind estimation and the truth values along with generated noise onto a single plot. A step input

of 5 knots is performed to show the response to dramatic changes. The performance measure is for the entire simulation.

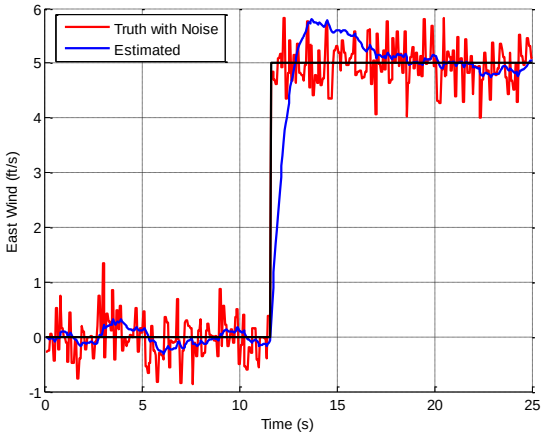

Figure 16: True Wind, Noise and Estimation of East Wind

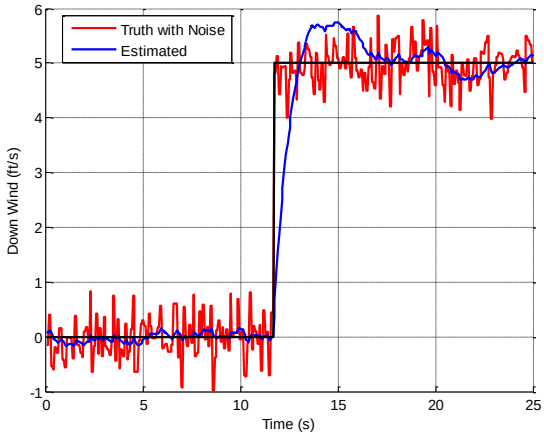

Figure 17: True Wind, Noise and Estimation of Down Wind

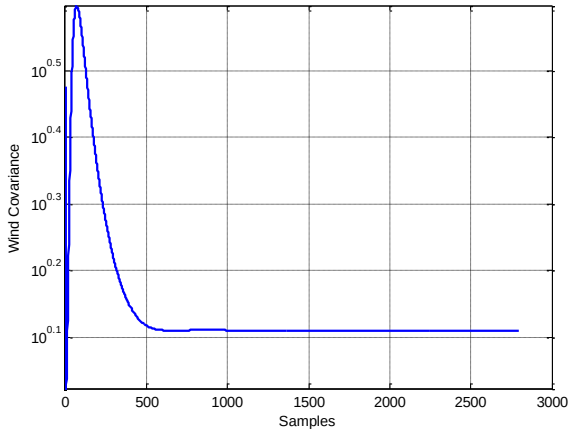

Figure 18: Performance Measure of EKF Simulation

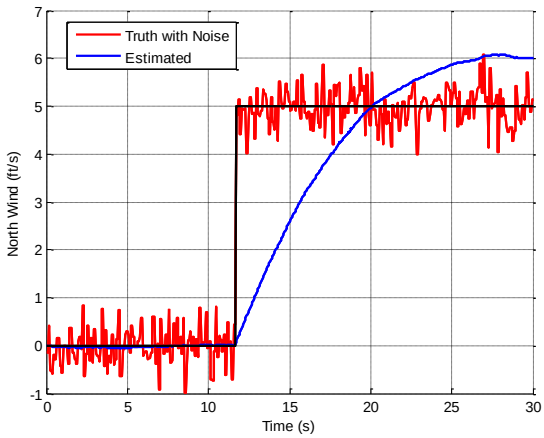

Figure 19: Ture Wind, Noise and Estimation of North Wind

It is found that the wind can accurately be estimated using this method for the crosswind and the downwind. The north wind is the tailwind component and is not as accurately estimated.

7.3 Longitudinal Guidance Simulation Results

The longitudinal guidance for landing employs a negative three percent glide slope followed by a flare maneuver at 52 feet. The altitude for this stage is slightly higher than

prescribed by the FAA but, due to the reaction time of the controller, it is necessary to begin the flare at this point. This allows time for the aircraft to flow into the landing smoothly and ground impact to be soft. The longitudinal flare is produced using the method described in chapter 3 section 3 and the results are presented in figures 20 and 21.

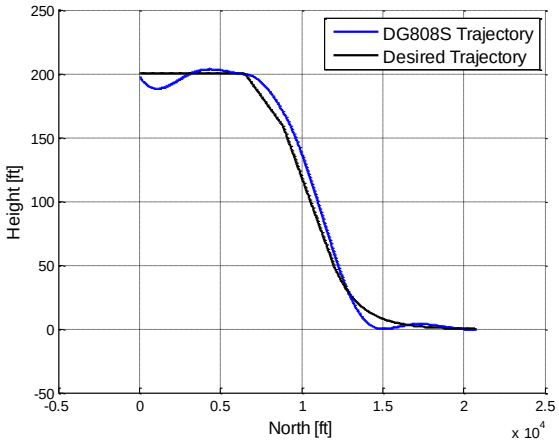

Figure 20: DG808S Landing Sequence

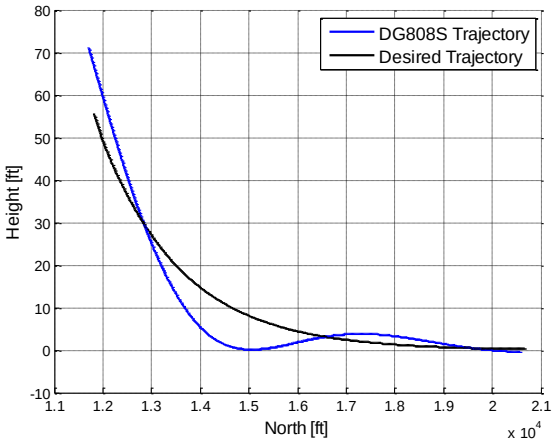

Figure 21: Flare Portion of Landing Sequence

The aircraft overshoots the desired flare path therefore must be started at a greater altitude than normally observed. The combination of height ($52\ ft$) and constant τ (565) when utilizing equation 3.5, allow the aircraft to overshoot without impacting the ground. Good planning could allow the aircraft to land at this point by using an altimeter and reducing the velocity once a specified altitude is reached. This would allow the aircraft to land earlier and further negate any lasting crosswind effects.

The states and controls that coincide with the flare maneuver are presented in figures 22 through 27.

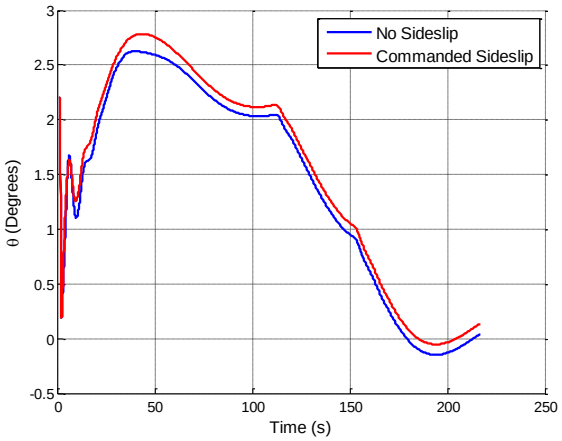

Figure 22: Pitch Angle for Full Flight Simulation

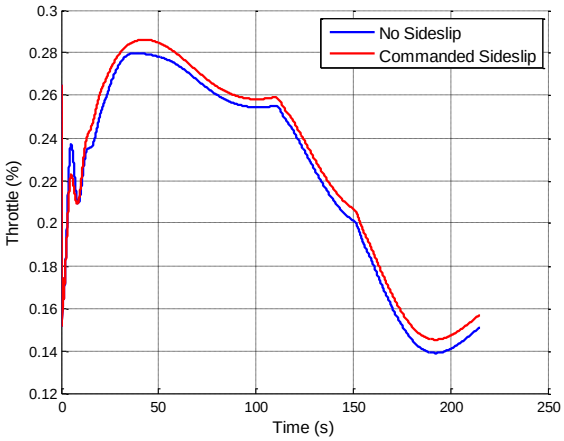

Figure 24: Throttle Percent for Full Flight Simulation

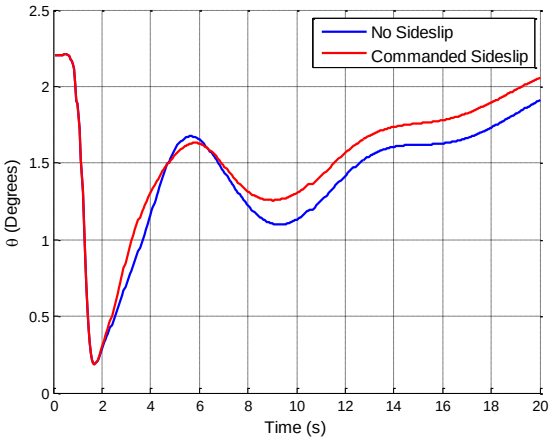

Figure 23: Pitch Angle for Initial 20 Seconds

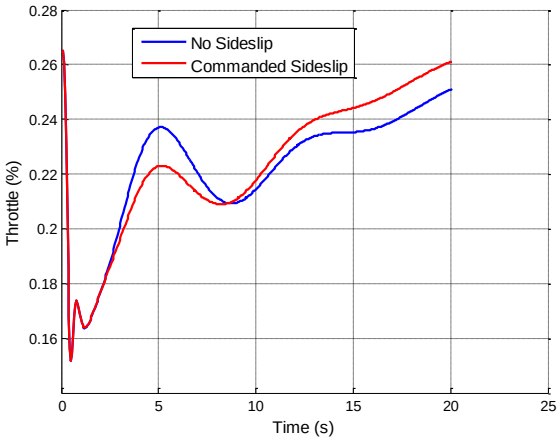

Figure 25: Throttle for Initial 20 Seconds

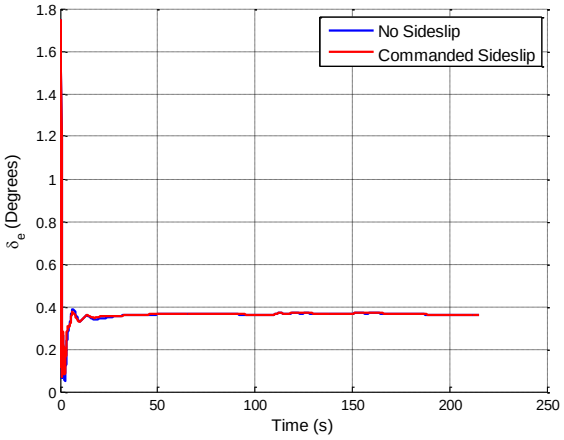

Figure 26: Elevator Command for Full Flight Simulation

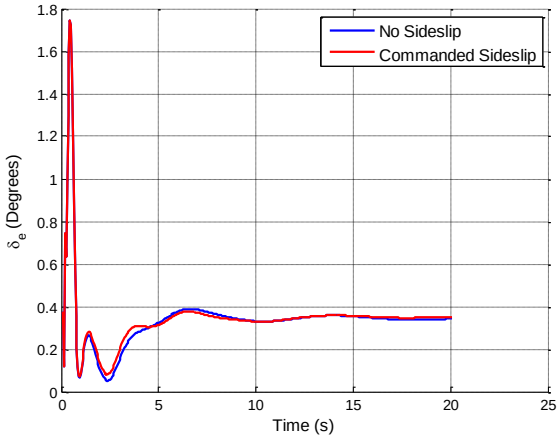

Figure 27: Elevator Deflection for Initial 20 Seconds

The figures on the left are the full simulation plots while the figures on the right only display 20 seconds of the simulation. Oscillations upon introduction of the autopilot are common however it should be noted that the response of the system should meet the requirements of the aircraft. The servo maximum frequency should not be exceeded by the controller and the maximum allowable structural loading should not be exceeded by response to these oscillations.

7.4 Lateral Directional Guidance Simulation Results

This section presents the lateral and directional guidance for the cruise and landing phases. The optimal K_β values for landing are determined with roll and crab constraints in sections 7.4.1 and 7.4.2 respectively. Gust analysis is performed for both optimization methods in 7.4 and 7.5.

7.4.1 Simulation of Cruise Phase for Constant Crosswind and Gust

The DG808S simulation is run with the NMPC and both sideslip compensation and no sideslip compensation for crosswind. When no sideslip is commanded the aircraft is pointed into the wind in a direction that will cause the aircraft to most efficiently fly along the trajectory provided by the guidance model given that there is zero sideslip. Different crosswind values are simulated starting at 0 and increasing by 5 to 15 knots. For the blue simulations the sideslip is commanded to 0 and the rudder is the only control surface countering the crosswind effects. This results in a wings level attitude, with only yaw compensation.

The second simulation is run with sideslip commanded using equation 7.1 to calculating the angle. Since sideslip is commanded, roll is used to compensate and remain on course. This

action causes a coordinated turn proportional to the estimated crosswind value. The same wind conditions are generated for both cases. For comparison purposes the two simulations are presented together. All control surfaces are started at zero and the aircraft is started at a height of 200 feet and offset 8 feet east of the desired trajectory at cruise speed of 35 knots. The value for K_β used, was chosen as the low value for gust conditions presented in section 7.6 and is 0.12 for cruise. The results of these simulations are presented in figures 28 through 31. The following symbol signifies the crosswind direction. ⇦

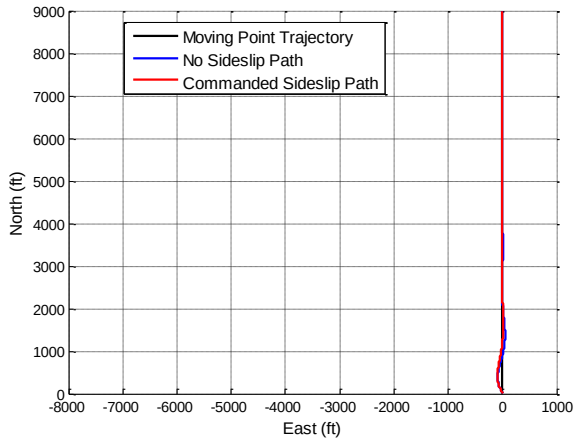

Figure 28: 15 Knot Constant Crosswind

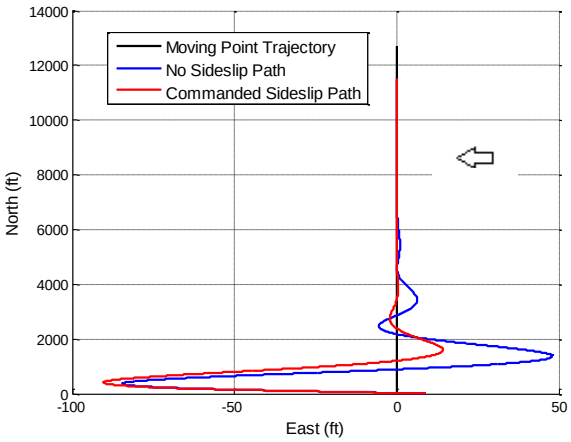

Figure 30: 15 Knot Constant Crosswind (Modified x-axis)

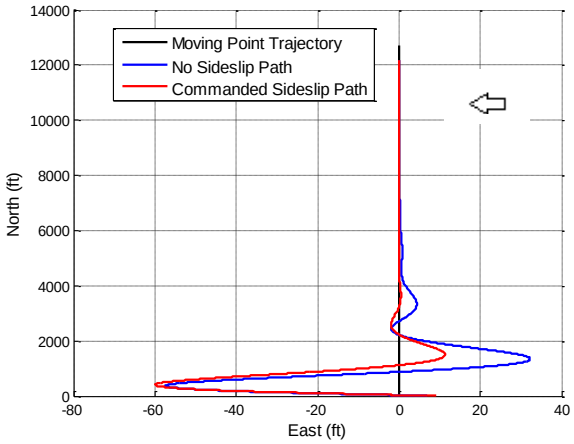

Figure 29: 10 Knot Constant Crosswind (Modified x-axis)

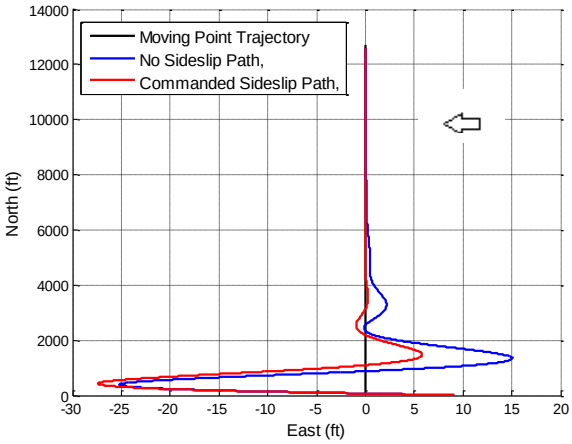

Figure 31: 5 Knot Constant Crosswind (Modified x-axis

Figure 28 presents the results of the 15 knot crosswind simulation with equivalent axis dimension. This shows that the deviation from the desired path is not great enough for evaluation. The subsequent plots have modified the x axis for adequate display. It can be seen that the trajectory of the commanded sideslip more closely follows and converges more quickly than the no sideslip path.

The states for a 10 knot crosswind simulation in the cruise phase are presented in figures 32 through 35.

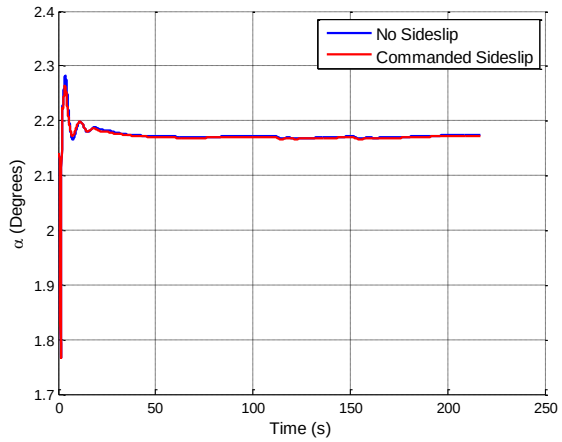

Figure 32: Angle of Attack for Constant Crosswind

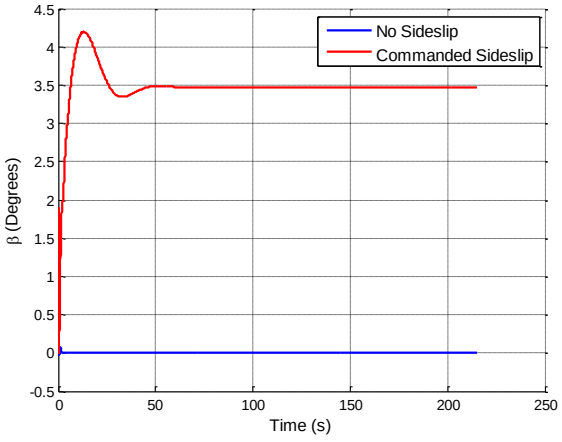

Figure 33: Sideslip Angle for Constant Crosswind

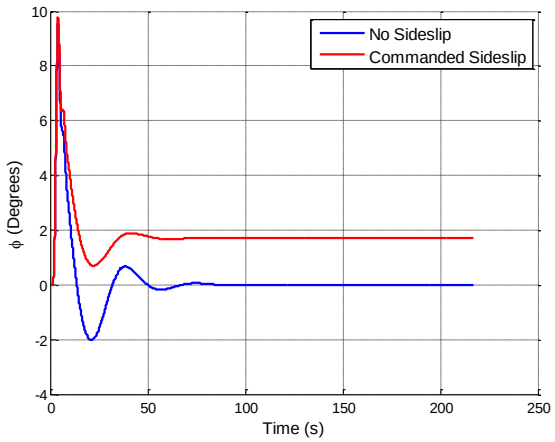

Figure 34: Roll Angle for Constant Sideslip

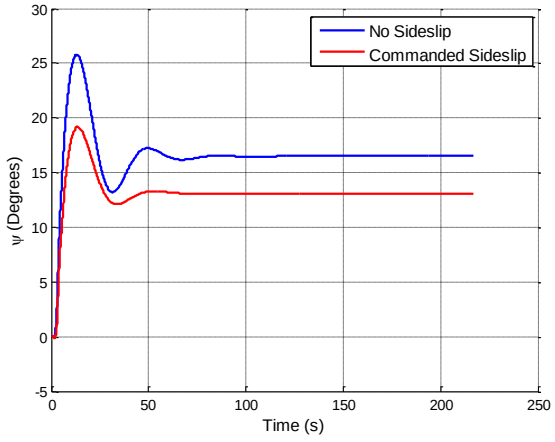

Figure 35: Yaw Angle for Constant Sideslip

The states reiterate the results of the path following. There are high oscillations when the controller is started. This is common however it is important to determine if the oscillations are outside the possible range of the aircraft. The angular rates of the aircraft are presented in figures 36 through 41.

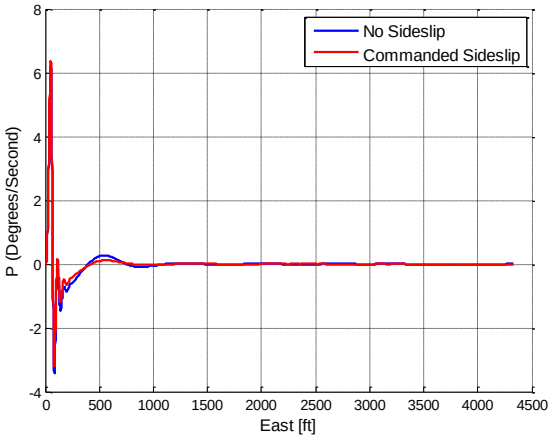

Figure 36: Roll Rate for Constant Crosswind

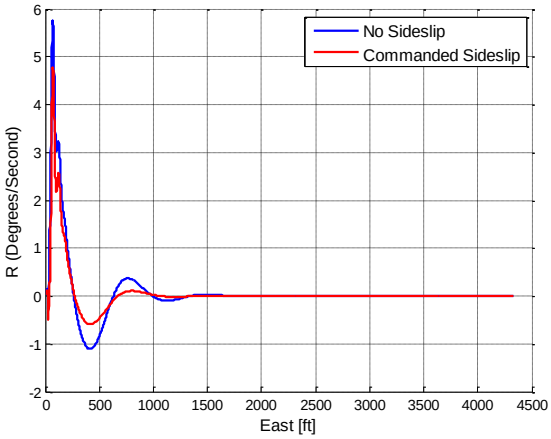

Figure 38: Yaw Rate for Constant Crosswind

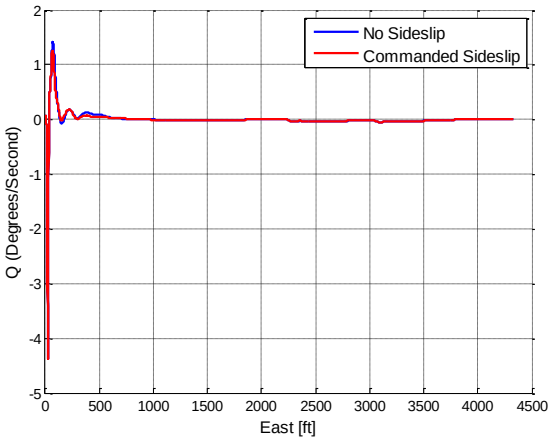

Figure 37: Pitch Rate for Constant Crosswind

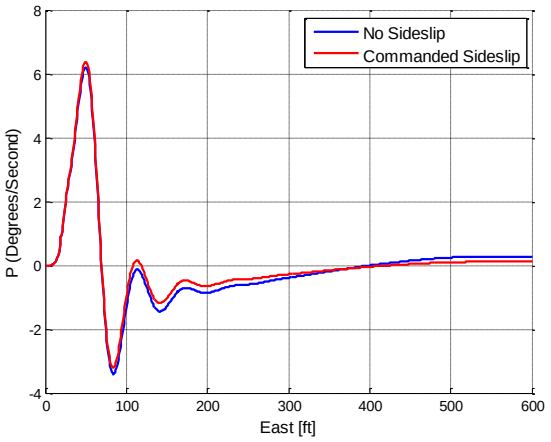

Figure 39: Roll Rate for Constant Crosswind

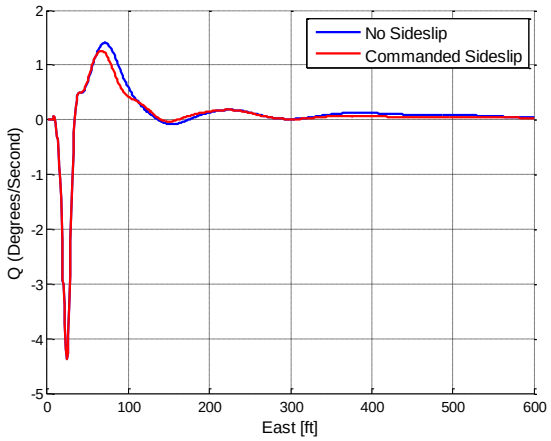

Figure 40: Pitch Rate for Constant Wind

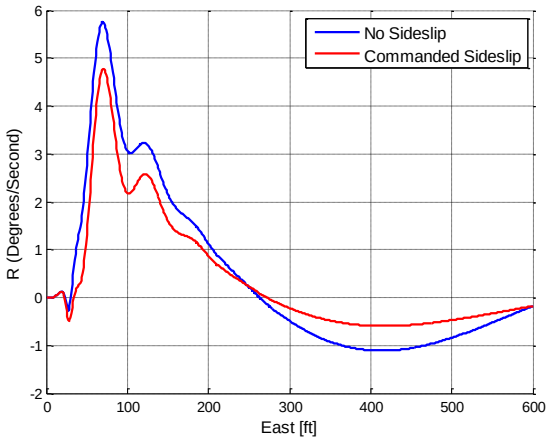

Figure 41: Yaw Rate for Constant Crosswind

The angular rates do not have high enough magnitude to cause any alarm with the structure of the aircraft. These are within typical bounds.

The controls for the 10 knot simulation are presented in figures 42 through 45.

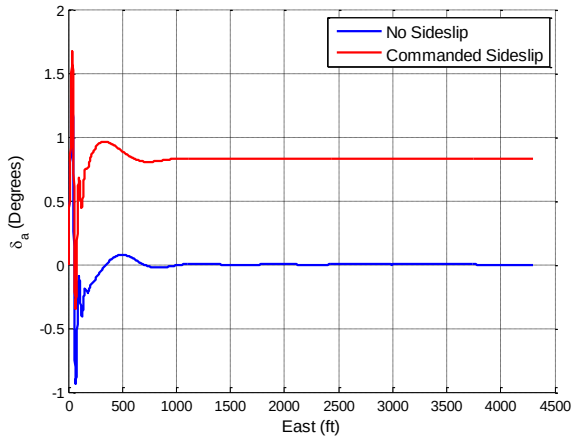

Figure 42: Aileron Deflection for Constant Crosswind

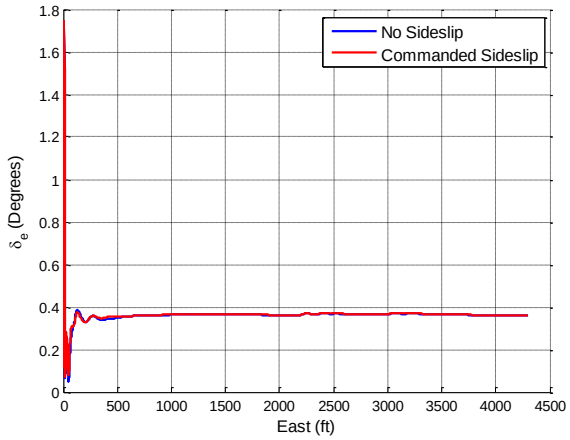

Figure 43: Elevator Deflection for Constant Crosswind

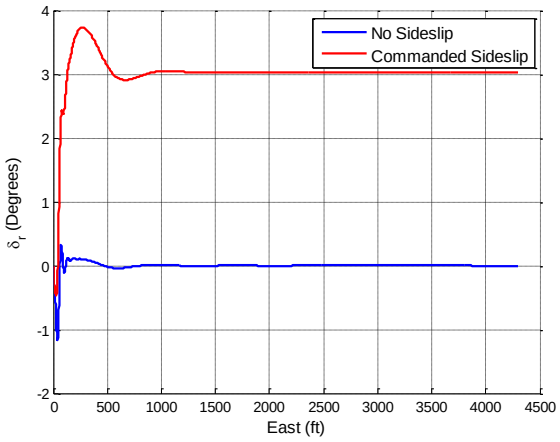

Figure 44: Rudder Deflection for Constant Crosswind

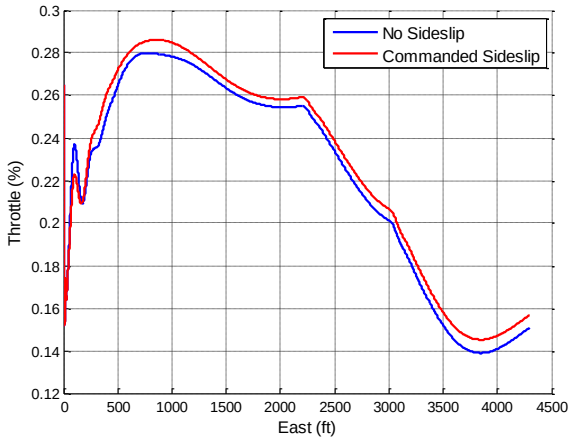

Figure 45: Throttle Percent for Constant Crosswind

The control plots show the expected behavior that the aileron and rudder are working together for a coordinated turn into the wind. It is important to note that the high oscillations at the beginning may have higher frequency than the servos on the aircraft. If this is the case the rates in the control must be adjusted.

Gust conditions are simulated using 2, 3, and 4 feet per second squared wind acceleration for time intervals that lead to 5, 10 and 15 knot maximum gust levels. This model is used as a generalization to show the autopilot response to wind gusts. This input is applied after the simulation has converged. No initial input deviations are shown. It can be seen that the coordinated response outperforms the single directional approach. The value for K_β used, was chosen as the low value for gust conditions presented in section 7.6 and is 0.12 for cruise. The results are presented in figures 46 through 49.

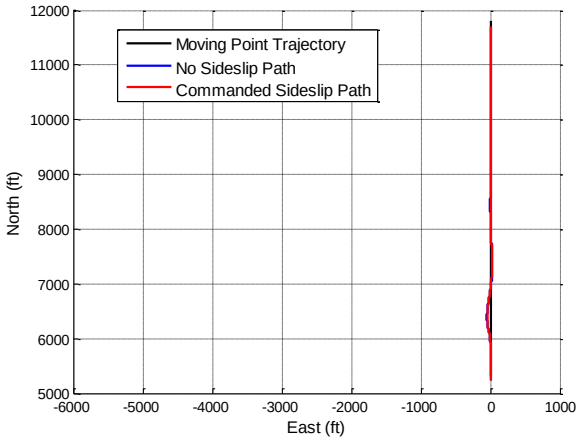

Figure 46: 15 Knot Crosswind Gust

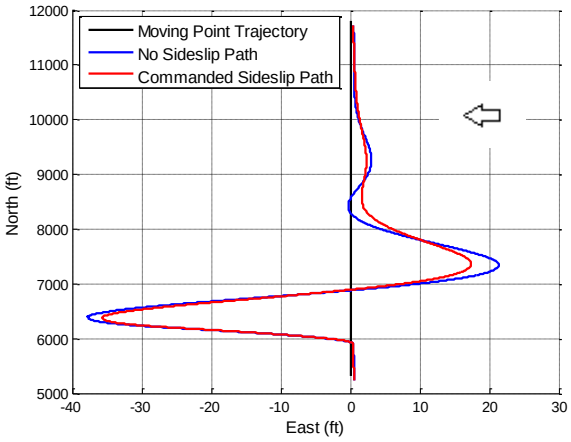

Figure 48: 10 Knot Crosswind Gust (Modified x-axis)

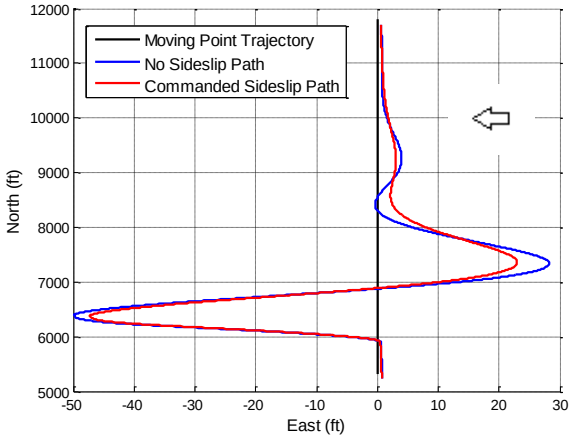

Figure 47: 15 Knot Crosswind Gust (Modified x-axis)

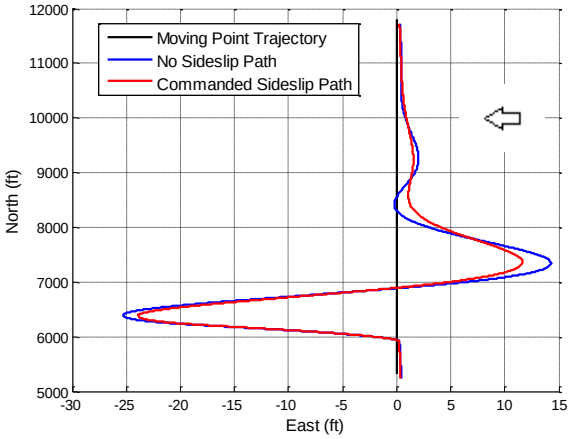

Figure 49: 5 Knot Crosswind Gust (Modified x-axis)

The states for wind crosswind gust condition are presented in figures 50 through 57.

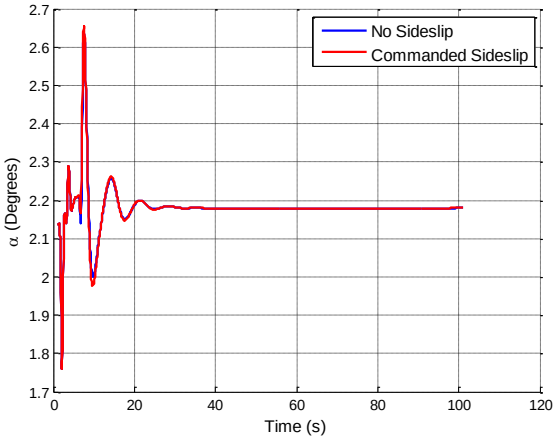

Figure 50: Angle of Attack for Gust Crosswind

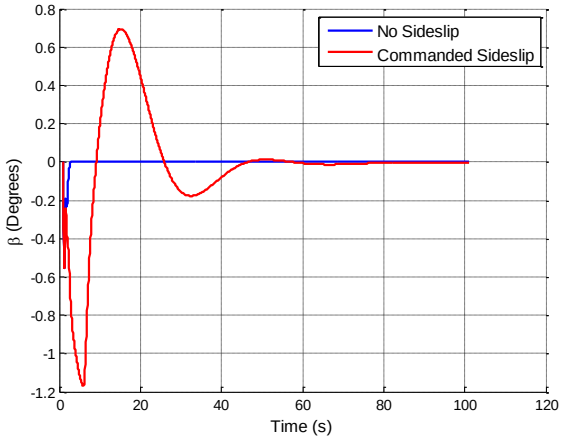

Figure 51: Sideslip Angle for Gust Crosswind

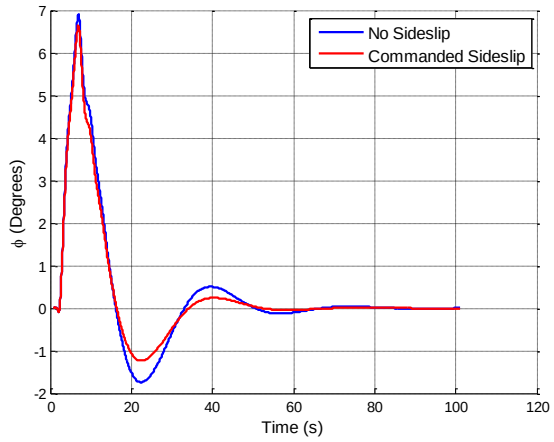

Figure 52: Roll Angle for Gust Crosswind

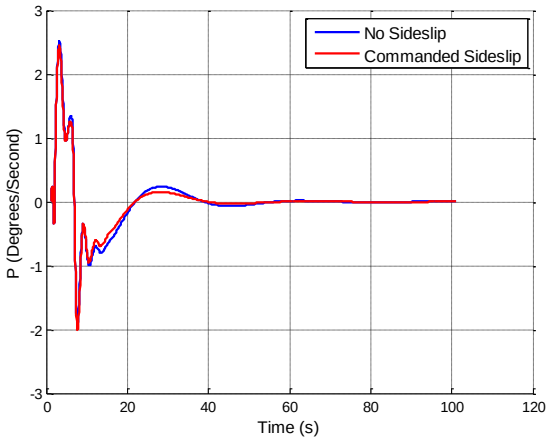

Figure 55: Roll Rate for Gust Crosswind

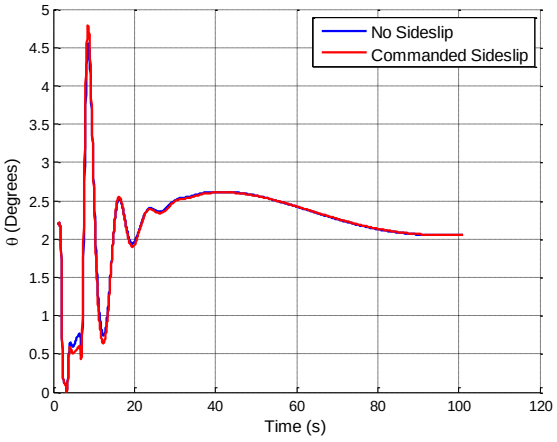

Figure 53: Pitch Angle for Gust Crosswind

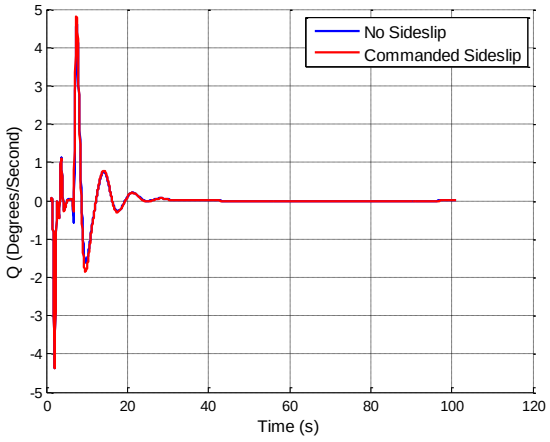

Figure 56: Pitch Rate for Gust Crosswind

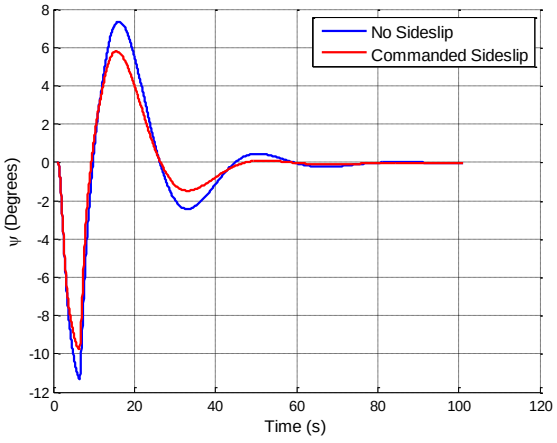

Figure 54: Yaw Angle for Gust Crosswind

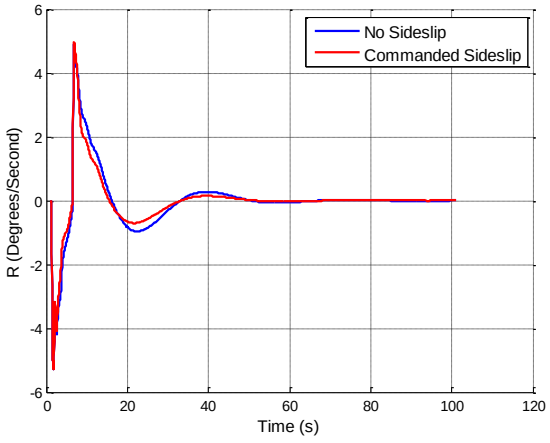

Figure 57: Yaw Rate for Gust Crosswind

This shows a decrease in yaw angle from 7.8 degrees to 6.2 degrees, which is a 25% decrease.

The initial roll angle is above 5 degrees for this gust of 10 knots. A gust of this magnitude would cause a wingtip strike for this aircraft therefore is out of the envelope for the landing phase. However, this would be perfectly adequate for cruise flight.

The commanded controls for 10 knot gusts are presented in figures 58 through 61.

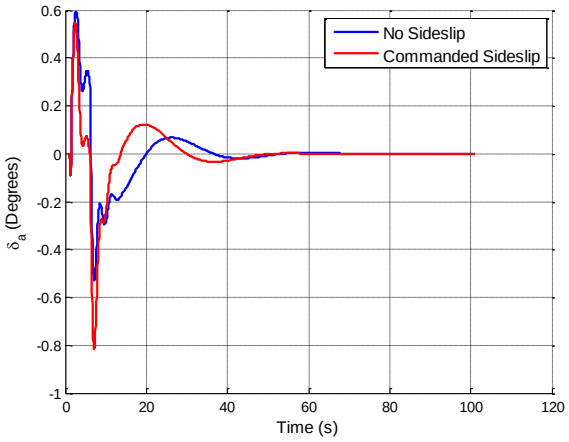

Figure 58: Aileron Deflection for Gust Crosswind

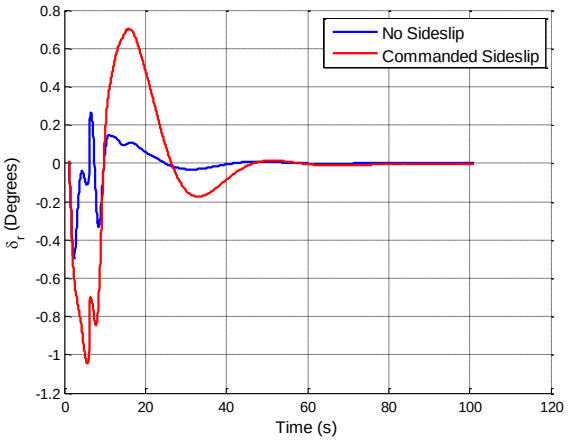

Figure 60: Rudder Deflection for Gust Crosswind

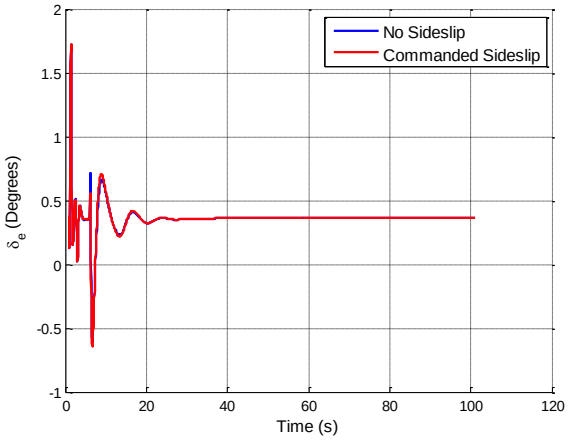

Figure 59: Elevator Deflection for Gust Crosswind

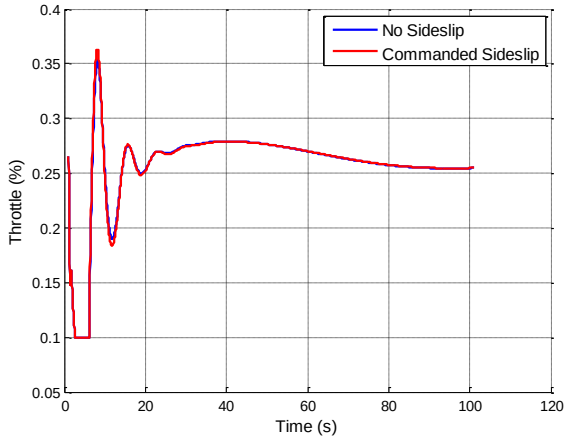

Figure 61: Throttle Percent for Gust Crosswind

The controls again are more responsive for the commanded sideslip which is to be expected.

7.4.2 Determination of Optimal K_β values for Best Results in the Landing Phase with Roll Constraint

The maximum allowable crosswind for landing according to the FAA is twenty percent V_{stall} [43]. This crosswind speed for the DG808S is determined to be 3.6 Knots. At this speed while using zero sideslip command the crab angle is 5.8 degrees. As the maximum allowable crab angle for the aircraft has not been determined experimentally, this value will be used. Since this is a generic model it can be implemented into any aircraft without loss of integrity.

The maximum allowable roll angle, due to geometric constraints, for the DG808S is five degrees. Because of the unpredictability the aircraft may roll more than five degrees. This would be unsafe and could result in a tip strike. A safety factor of 1.5 is incorporated for uncertainty and the maximum gust allowance for each instance will be tabulated in the next section.

$$0.20V_{stall} = \xi_{max_{land}} = 5.8^\circ \quad [7.1]$$

$$\phi_{max_{land}} = \frac{5^\circ}{1.5} = 3.33^\circ \quad [7.2]$$

The roll constraint for the optimization process is now set at 3.33°. Increasing the K_β until a roll angle of $3.33^\circ$is achieved, the yaw angle becomes -0.5 and $K_\beta = 1.2$. For a crosswind value of 3.6 knots and a roll angle of 3.33° the yaw angle goes negative to compensate for a roll angle that is too large. This is generated due to a K_β value that is too high. This is mitigated by decreasing K_β thus decreasing roll angle to achieve a yaw angle of zero. At zero yaw the roll angle is 2.8°. This is the optimal K_β for a crosswind of 3.6 Knots with roll constraint. The process is repeated for increasing crosswind until all constraints are met i.e. $\xi_{max_{land}} = 5.8^\circ$ and $\phi_{max_{land}} = 3.33^\circ$. The results are presented in the figure below.

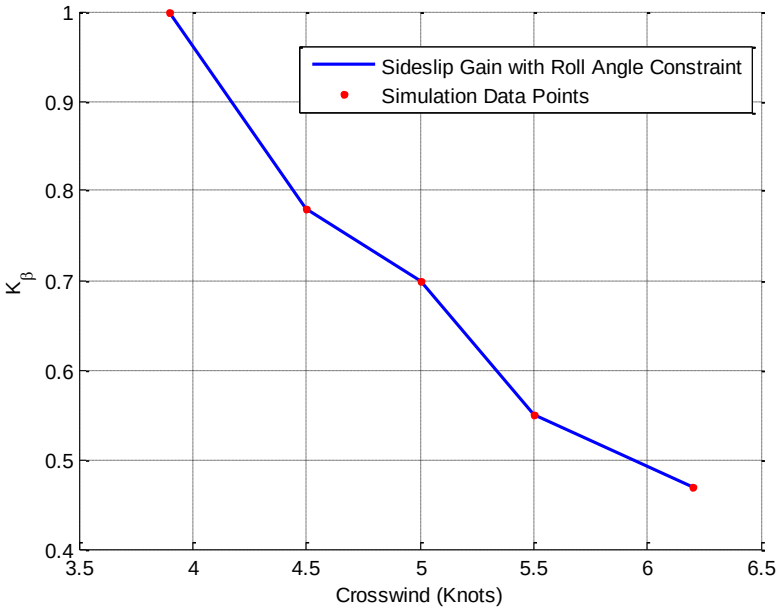

Figure 62: Sideslip Gain Determined by Constraining the Roll Angle to 3.3 Degrees

This figure is used to determine the optimal K_β value for the DG808S given prior knowledge of the crosswind conditions for flight.

7.5 Determination of Optimal K_β values for Best Results in the Landing Phase with Crab Angle Constraint

The same procedure for finding K_β from section 7.4 is performed, however the crab angle is set as the constraint while the roll angle is allowed to vary.

The crab angle is set as a constraint at a maximum of 3.9 degrees using a factor of safety of 1.5. The roll angle is set to not exceed the maximum allowable angle of 3.3 as determined by the geometry of the aircraft. The results are presented in figure 63.

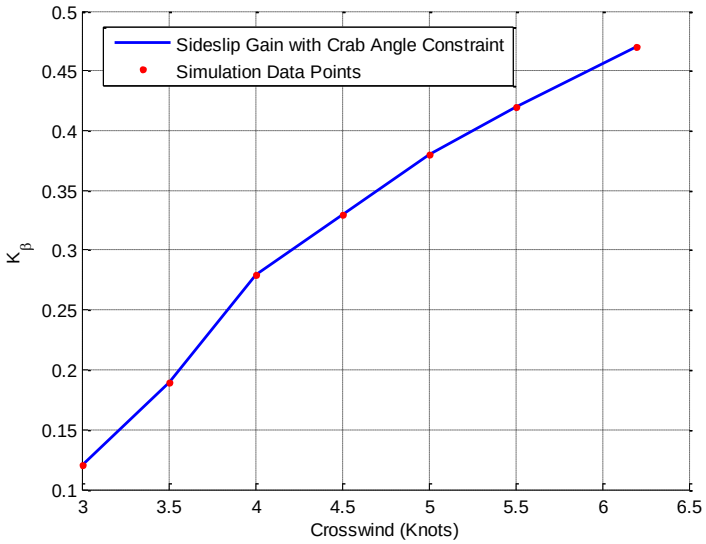

Figure 63: Sideslip Gain Determined by Constraining the Crab Angle to 3.9 Degrees

7.6 Gust Rejection with Crab Angle Constraint

The K_β values are determined for constant crosswind and an allowance remains for gust. In this section a gust allowance is tabulated for each instance of K_β that was determined in the previous section. The simulated maximum gust allowance is the peak velocity in knots generated by a constant acceleration for 1.6 seconds. The roll angle is constrained at 3.3 degrees and the gust alters this value. Since the crab angle is relatively low the un-commanded constraint applies to roll. When the maximum allowable roll of 5 degrees is attained the maximum allowable gust is determined. The results are presented in table 6.

Table 6: Gust Compensation with Roll Angle Constraint

Crosswind (KTS)	K_β	Crab Angle Reaction (Degrees)	Crab Angle Uncommanded (Degrees)	Max Gust (KTS)
3.9	1.00	0.0	-2.0	2.3
4.5	0.78	1.0	-1.1	2.2
5.0	0.70	2.2	-0.7	2.0
5.5	0.55	2.8	0.3	2.0
6.2	0.47	3.9	1.6	2.0

The optimal K_β gives the lowest crab angle for the expected constant crosswind. If the gusts are higher than the allowable for this setting then K_β must be reduced. This increases the crab angle but allows more roll authority to counter the effects of crosswind gusts. While the crab angle increases it is important to remain below the threshold of 5.8 degrees for this vehicle. At a particular K_β the crab angle, rather than the roll angle, will become the larger value and at this point the crab angle should be used as the constraint. Since the constraint is initially determined by the geometry of the aircraft it may not be possible to switch to the other constraint. Prior to flight, simulations should be run to determine if the best K_β for the expected crosswind gust has been chosen.

Table 7: Gust Compensation with Crab Angle Constraint

Crosswind (KTS)	K_β	Bank Angle Reaction (Degrees)	Crab Angle Uncommanded (Degrees)	Max Gust (KTS)
3	0.12	0.5	-3.5	5
3.5	0.19	0.8	-2.7	4.7
4.0	0.28	1.4	-1.7	4.1
4.5	0.33	1.8	-0.9	3.6
5.0	0.38	2.2	-0.2	3.2
5.5	0.42	2.6	0.3	2.7
6.2	0.47	3.2	1.6	2.0

Chapter 8

Procedure for Implementation of Landing Sequence for a Generic UAS

This section presents a procedure for implementation of this method for a generic UAS.

- Verify that all FAA regulations for safe landing of aircraft are met
- Use aircraft geometry and control surface constraints to define landing limitations
- Based on aircraft geometry, determine if the aircraft should use K_β values based on roll or yaw constraints
- By setting either roll or yaw as the constraint create K_β table for aircraft from simulation
- Look up wind direction and magnitude for flight time
- Use K_β table to determine optimal K_β value
- Run flight simulation with K_β and adjust if expected gusts are too high
- Load K_β into flight guidance prior to take off

Chapter 9

Summary and Conclusions

- A wind estimation EKF was successfully implemented in an over the horizon autopilot.
- A modified gain scheduling technique was used to optimize aircraft attitude based on crosswind estimation while using aircraft geometry as constraint.
- During the cruise flight a value for 0.12 was used for K_β. This value was chosen as the first value that was encountered in the crosswind and gust study. It was also noticed that, although low values for K_β resulted in better trajectory tracking, high values more quickly responded to wind but were slow to converge to the commanded trajectory.
- Utilizing multiple control surfaces during flight in crosswind decreases the time for trajectory convergence. Multiple control surface use causes a coordinated turn that more efficiently counters the effect of crosswind than simply using rudder alone. This also more quickly rejects the effects of wind gust.

For the cruise flight phase there were dramatic reductions in both divergence from the desired path and in time to converge on the desired path. Most savings were seen after the initial reaction to the crosswind. The initial deviation savings were negligible however upon return to the path the 0 commanded sideslip condition had a tendency to overshoot the path by a large margin while the commanded sideslip condition dramatically reduced this overshoot. The commanded sideslip condition also converged to the desired path much more quickly in the constant wind condition. The results are presented in tables 8 and 9.

Table 8: Cruise Flight with Constant Crosswind Overshoot and Convergence

Condition	15 Knots	10 Knots	5 Knots
Overshoot Reduction	68	68	60
Convergence Improvement	53	33	33

Table 9: Cruise Flight with 10 Knot Gust Overshoot and Convergence

Condition	15 Knots	10 Knots	5 Knots
Overshoot Reduction	18	18	14
Convergence Improvement	0	0	0

Table 10 shows the percent savings of the total error calculated along the trajectory shown in the constant and gust conditions figures. The total error is calculated by summing the error from the desired path for the commanded and un-commanded sideslip conditions, then subtracting the totals. The percentage is calculated by subtracting the ratio from 1 and multiplying by 100.

$$e_t = 100\left(1 - \frac{|P_{cmd} - P_d|}{|P_o - P_d|}\right)$$

Where P_{cmd}, P_d, P_0 are the east point values for the sideslip commanded path, the desired path and the 0 sideslip commanded path. e_t is the total error savings in percent.

Table 10: Increased Performance with Addition of Sideslip Command on Constant and Gust Crosswind Conditions

Crosswind Speed (KTS)	Constant Crosswind Performance (%)	Gust Crosswind Performance (%)
15	22.7	5.7
10	22.6	5.7
5	19.9	5.7

It should also be noted that there are energy savings associated with all reductions in overshoot and trajectory tracking.

The maximum landing operations for the DG808S under autopilot control are predicted allowing a maximum crab angle of 2 degrees. Given this condition the results are presented in table 11.

Table 11: Maximum Conditions for Landing of the DG808S

Constant Crosswind (KTS)	Gust (KTS)	K_β
3.9	2.3	0.78

Because of the in-line landing gear and limited crab angle these results are calculated using the sideslip method. The crab angle is set to 0 degrees and allowed to change up to 2 degrees based on gust. This is an increase in crosswind of 2.6 knots from the 0 beta commanded value. The cruise phase was tested under maximum allowable conditions at 15 knots. Beyond this the aircraft diverged from the desired trajectory.

Chapter 10

Recommendations and Future Work

- Discover an optimal cruise flight K_β for trajectory tracking by performing a similar study for the cruise phase of flight.
- Collect experimental data on the DG808S to determine the maximum allowable crab angle upon landing.
- Update the controller to have an undefined speed enabling the speed to be reduced and to increase longitudinal tracking in high wind conditions. Perform similar analysis for multiple speeds.
- Perform similar analysis for different aircraft to show generalization.
- Real-time calculation of K_β may produce optimal flight throughout each phase. Implement this through a simulation of all phases of flight.

The velocity used in this simulation is 35 Knots. The FAA recommended velocity for commercial aircraft is $1.3V_{Stall}$. For the DG808S this is approximately$13\ Knots$. A complete simulation at low speed for this aircraft is currently not possible. An accurate dynamic model at such a low speed has not been developed. System identification should be used to determine the aircraft dynamics at this speed. This method is generic and may be applied to any aircraft at any speed with a similar guidance.

References

[1] “Flight Safety Digest” Flight Safety Foundation. November-December 1998. January-February 1999.

[2] Kargin, Volkan. “Design of an Autonomous Landing Control Algorithm for a Fixed Wing UAV”. Middle East Technical University. October 2007.

[3] Silva, Joao. “Development and Design of the Landing and Guidance and Control System for the S20 UAV”. Instituto Superior Tecnico. 1049-001 Lisboa, Portugal. November, 2014.

[4] Nickol, Craig L. Guynn, Mark D. Kohout, Lisa L. Ozoroski, Thomas A. “High Altitude Long Endurance Air Vehicle Analysis of Alternatives and Technology Requirements Development”. NASA/TP-2007-214861. March 2007.

[5] Wang, Show-Tien. Frost, Walter. “Atmospheric Turbulence Simulation Techniques with Application to Flight Analysis”. NASA Contractor Report 3309. NAS8-32692 September, 1980.

[6] Justus, C.G. Campbell, C.W. Doubleday, M.K. Johnson, D.L. “New Atmospheric Turbulence Model for Shuttle Applications”. NASA Technical Memorandum 4168. January 1990.

[7] Hu, Qian. Hu, Chen, Kongkun. Tao, Yubo. Yang, Ruixi. Wang, Ling. Hu, Pan. “Wind Speed Spatio-temporal Forecasting of Wind Farms Based on Universal Kringing and Bayesian Dynamic Model”. IEEE International Conference on Power System Technology. Oct. 20-22, 2014.

[8] Ambach, Daniel. Schmid, Wolfgang. “Spatio-temporal Wind Speed Predictions for Germany” Department of Statistics European University. Frankfurt, Germany. GRASPA June 15-16, 2015.

[9] Imai, Toshiaki. Kusunoki, Kenichi. Yoshihiro, Hono. Takemi, Tetsuya. Araki, Keiji. Fukuhara, Takaaki. Bessho, Kotaro. Hoshino, Shunuske. Shibata, Toru. “Spatial Correlation and Temporal

Fluctiuations of Wind Velocities Observed on a Plain Field". The Seventh Asia-Pacific Conference on Wind Engineering. Taipei, Taiwan. November 8-12, 2009.

[10] "Cross with Care". Business & Commercial Aviation. June 2015.

[11] Durden, Rick. "Anatomy of a Crosswind Landing". Aviation Safety. Vol. 29. Num. 3. March, 2009.

[12] Lagelaan, Jack W. Alley, Nicholas. Neidhoefer, James. "Wind Field Estimation for Small Unmanned Aerial Vehicles" AIAA *Guidance, Navigation and Control Conference*, Toronto, Canada. 2010-8177.

[13] Garcia, Gonzalo. Keshmiri, Sharaiar. "Design and Application of an Extended Kalman Filter in a Flight Control System Development" AIAA *InfoTech@Aerospace*. St. Louis, Mo. 2011.

[14] Langelaan, Jack W. Splatzer, John. Montella, Corey. Joachim, Grenestedt. "Wind Field Estimation for Autonomous Dynamic Soaring". IEEE *International Conference on Robotic Soaring*. April 2012.

[15] Wagner, Thomas. Valasek, John. "Digital Autoland Controls Laws Using Quantitative Feedback Theory and Direct Digital Design". *Journal of Guidance, Control and Dynamics*, Vol. 30, No. 5, September-October 2007.

[16] Woodbury, Timothy. Valasek, John. "Synthesis and Flight Test of an Automatic Landing using Quantitative Feedback Theory". AIAA *SciTech. Guidance, Navigation and Control*. Kissimmee, FL. 5-9 January, 2015.

[17] Choi, Hyoung. Lee, Sangjong. Lee, Jangho. Kim, Eung Tai. Shim, Hyunchul. "Aircraft Longitudinal Auto-landing Guidance Law using Time Delay Control Scheme". *Trans. Japan Soc. Aero. Space Sci*. Vol. 53, No. 181, p. 207-214, 2010.

[18] Raj, K. David Solomon. Tattikota, Goutham. “Design of Fuzzy Logic Controller for Auto Landing Applications*”. Internatonal Journal of Scientific and Research Publications*, Vol. 3, Iss. 5, May 2013.

[19] Dong Il, You. Yeon Deuk, Jung. Sung Wook, Cho. Hee Min, Shin. Sang Hyup, Lee. Hyunchul Shim, David. “A Guidance and Control Law for Precision Automatic Take-Off and Landing of Fixed-Wing UAVs”. AIAA *Guidance*, *Navigation*, *and Control Conference* 13-16 August 2012, Minneapolis, Minnesota.

[20] Rosa, Paulo. Silvestre, Carlos. Cabecinhas, David. Cunha, Rita. “Autolanding Controller for a Fixed Wing Unmanned Air Vehicle”. AIAA *Guidance, Navigation and Control Conference*. 20-23 August 2007, Hilton Head, South Carolina.

[21] Saini, Gaurav. Balakrishnan, S.N. “Adaptive Critic Based Neurocontroller for Autolanding of Aircrafts with Varying Glideslopes”. Department of Mechanical and Aerospace Engineering and Engineering Mechanics, University of Missouri-Rolla. MO.

[22] Grillo, Caterina. Montano, Fernando. “Gain Scheduling Automatic Landing System by Modeling Ground Effect”. *International Journal of Engineering Inventions*. Vol. 4, Iss. 6, November, 2014. p. 44-51.

[23] Short Landing Requirements

[24] Balmer, Georg Robert. “Modelling and Control of a Fixed-Wing IAV for Landings on Mobile Landing Platforms”. KTH Royal Institute of Technology. Stockholm, Sweden. Oct. 29, 2015.

[25] Yoon, Seungho. Kim, Jin H. Kim, Youdan. “Spiral Landing Trajectory and Pursuit Guidance Law Design for Vision-Based Net-Recovery UAV”. AIAA *Guidance, Navigation and Control Conference*. 10-13 August 2009, Chicago, Illinois.

[26] Riseborough, P. “Automatic Take-Off and Landing Control for Small UAV’s”. BAE SYSTEMS Melbourne, Australia.

[27] Williams, Paul. Crump, Michael. “Intelligent Landing System for Landing UAVS at Unsurveyed Airfields”. BAE Systems, Australia. ICAS. 2012.

[28] Kong, Weiwei. Zhou, Dianle. Zhang, Daibing. Zhang, Jianwei. “Vision-based Autonomous Landing System for Unmanned Aerial Vehicle: A Survey”. College of Mechatronic Engineering and Automation. National University of Defense and Technology. Hunan, China. University of Hamburg. Hamburg, Germany.

[29] Reynolds, Adam. “Drone On – Motion Control for UAVs”. EDN network. January 20, 2015.

[30] Menon, P.K. Vaddi, S.S. Sengupta, P. “Robust Landing-Guidance Law for Impaired Aircraft”. *Journal of Guidance, Control, and Dynamics*. Vol. 35, No. 6, November-December 2012.

[31] Fitzgerald, Daniel L. Mejias, Luis. Eng, Pillar C. Liu, Xi. Walker, Rodney A. “Towards Flight Trials for an Autonomous UAV Emergency Landing Using Machine Vision”. *Australasian Conference on Robotics and Automation*. Brisbane, Australia. 10-12 December, 2007.

[32] Shah, M. Zamurad. Samar, Raza. Bhatti, I Aamer. “Lateral Track Control of UAVs using the Sliding Mode Approach: from Design to Flight Testing”. SAGE. *Transactions of the Institute of Measurement and Control.* 1-18. 2014.

[33] Xiong, Hua. Yi , Jian-qiang. Fan, Guo-liang. Jing, Feng-shi. “Anti-crosswind Autolanding of UAVs based on Active Disturbance Rejection Control”. AIAA *Guidance, Navigation and Control Conference*. 2-5 August 2010, Toronto, Canada.

[34] Mengen-Hohentengen. Friedeman Kuster DG808 D-KFFK albspotter. http://www.flickriver.com/photos/albspotter/3791447257/

[35] Stengel, Robert F. Flight Dynamics. Princeton University Press. Princeton, New Jersey. 2004.

[36] Lenschow, D.H. Spyers-Duran, P. "Measurement Techniques: Air Motion Sensing". NCAR Research Aviation Facility Bulletin No. 23. November 1989.

[37] Advanced Aircraft Analysis V3.6, Design, Analysis and Research Coorporation 20015.

[38] Design, Analysis and Research Coorporation. http://www.darcorp.com/

[39] Procedures and Techniques. Crosswind Landings.

http://code7700.com/crosswind_landing.html

[40] Sbalbi, Gabriele Fabrizio. "Wind and Water". June, 2014.

http://kitesurfculture.blogspot.com/2014/06/kitesurf-line-length-and-kite-behavior.html

[41] Flight Operations Briefing Notes. "Landing Techniques: Crosswind Landings". Approach and Landing Accident Reduction. Airbus. Flight Safety Foundation March. 2008.

[42] Cashman, Captain John. "Crosswind Guidelines". Boeing Commercial Airplanes. Seattle WA.

[43] Federal Regulations Title 14-Chapter 1-Subchapter C-Part 23. Federal Aviation Administration. U.S. Government Publishing Office. July 27, 2016.

[44] Ojha, S.K. Flight Performance of Aircraft. AIAA Education Series. J.S. Przemieniecki. Air Force Institute of Technology. Wright Patterson Air Force Base, Ohio. 1995.

[45] Flight Safety Foundation Approach and Landing Accident Reduction. FSF ALAR Briefing Note 8.3-Landing Distances. Flight Safety Digest. 8-12, 2000.

http://flightsafety.org/files/alar_bn8-3-distances.pdf

[46] Mayne, D. Q., Rawlings, C., Rao, C., and Scokaert, P. O. M., "Constrained Model Predictive Control: Stability and Optimality," Automatica, Vol. 36, No. 6, 2000.

[47] Bemporad, A., and Morari, M., Robustness in Identification and Control, Springer, London, 1999, Chap. 7.